# The ionospheric effects of the 2022 Hunga Tonga Volcano eruption and the associated impacts on GPS Precise Point Positioning across the Australian region

Brett Anthony Carter[1], Rezy Pradipta[2], Tam Dao[1], Julie Louise Currie[1], Suelynn Choy[1], Philip James Wilkinson[3], Phillip Stephen Maher[4], Richard Alexander Marshall[5], Ken Harima[6], Minh LeHuy[7], Thang Nguyen Chien[8], T. Nguyen Ha[9], and Trevor J. Harris[10]

[1]RMIT University
[2]Boston College
[3]IPS Radio and Space Services
[4]Space Weather Services, Australian Bureau of Meteorology
[5]Australian Bureau of Meteorology
[6]FrontierSI
[7]Institut De Physique Du Globe De Paris
[8]Institute of Geophysics
[9]Institute of Geophysics, VAST
[10]Defence Science & Technology Group

March 13, 2023

**Abstract**

The Hunga Tonga Volcano eruption launched a myriad of atmospheric waves that have been observed to travel around the world several times. These waves generated Traveling Ionospheric Disturbances (TIDs) in the ionosphere, which are known to adversely impact radio applications such as Global Navigation Satellite Systems (GNSS). One such GNSS application is Precise Point Positioning (PPP), which can achieve cm-level accuracy using a single receiver, following a typical convergence time of 30 mins to 1 hour. A network of ionosondes located throughout the Australian region were used in combination with GNSS receivers to explore the impacts of the Hunga-Tonga Volcano eruption on the ionosphere and what subsequent impacts they had on PPP. It is shown that PPP accuracy was not significantly impacted by the arrival of the TIDs and Spread-F, provided that PPP convergence had already been achieved. However, when the PPP algorithm was initiated from a cold start either shortly before or after the TID arrivals, the convergence times were significantly longer. GNSS stations in northeastern Australia experienced increases in convergence time of more than 5 hours. Further analysis reveals increased convergence times to be caused by a super equatorial plasma bubble (EPB), the largest observed over Australia to date. The EPB structure was found to be ˜42 TECU deep and ˜300 km across, traveling eastwards at 30 m/s. The Hunga Tonga Volcano eruption serves as an excellent example of how ionospheric variability can impact real-world applications and the challenges associated with modeling the ionosphere to support GNSS.

# The ionospheric effects of the 2022 Hunga Tonga Volcano eruption and the associated impacts on GPS Precise Point Positioning across the Australian region

**B. A. Carter[1], R. Pradipta[2], T. Dao[1], J. L. Currie[1], S. Choy[1], P. Wilkinson[3], P. Maher[4,5], R. Marshall[4], K. Harima[6], M. LeHuy[7], T. Nguyen Chien[7], T. Nguyen Ha[7], T. J. Harris[8]**

[1]School of Science, RMIT University, Melbourne, Australia
[2]Institute for Scientific Research, Boston College, Boston, USA
[3]Ionospheric Prediction Service (retired), Sydney, Australia
[4]Space Weather Services, Bureau of Meteorology, Sydney and Adelaide, Australia
[5]Now at: Riverbed Technology, Australia
[6]FrontierSI, Melbourne, Australia
[7]Institute of Geophysics, Vietnam Academy of Science and Technology (VAST), Hanoi, Vietnam
[8]School of Physical Sciences, The University of Adelaide, Adelaide, Australia

**Key Points:**

- PPP convergence times across northern Australia were significantly impacted in the hours after the eruption
- Extended periods of enhanced ROTI were the cause of convergence time increases
- A super equatorial plasma bubble, the largest observed over Australia, was responsible for PPP convergence time increases after the eruption

Corresponding author: Brett Carter, `brett.carter@rmit.edu.au`

## Abstract

The Hunga Tonga Volcano eruption launched a myriad of atmospheric waves that have been observed to travel around the world several times. These waves generated Traveling Ionospheric Disturbances (TIDs) in the ionosphere, which are known to adversely impact radio applications such as Global Navigation Satellite Systems (GNSS). One such GNSS application is Precise Point Positioning (PPP), which can achieve cm-level accuracy using a single receiver, following a typical convergence time of 30 mins to 1 hour. A network of ionosondes located throughout the Australian region were used in combination with GNSS receivers to explore the impacts of the Hunga-Tonga Volcano eruption on the ionosphere and what subsequent impacts they had on PPP. It is shown that PPP accuracy was not significantly impacted by the arrival of the TIDs and Spread-F, provided that PPP convergence had already been achieved. However, when the PPP algorithm was initiated from a cold start either shortly before or after the TID arrivals, the convergence times were significantly longer. GNSS stations in northeastern Australia experienced increases in convergence time of more than 5 hours. Further analysis reveals increased convergence times to be caused by a super equatorial plasma bubble (EPB), the largest observed over Australia to date. The EPB structure was found to be ∼42 TECU deep and ∼300 km across, traveling eastwards at 30 m/s. The Hunga Tonga Volcano eruption serves as an excellent example of how ionospheric variability can impact real-world applications and the challenges associated with modeling the ionosphere to support GNSS.



## Plain Language Summary

Global Navigation Satellite System (GNSS) applications permeate modern society, with many industry sectors heavily relying on precision satellite positioning, navigation and timing. Precise Point Positioning (PPP) is an advanced positioning technique that can achieve cm-level accuracy without the need for nearby reference stations. However, the time that it takes for the PPP solution to 'converge' is typically in the range of 10s of mins to hours, limiting the widespread uptake of PPP. There are numerous previous reports of waves and disturbances in the ionosphere, which are known to adversely impact GNSS applications. In this study, the impact of the disturbances in the ionosphere caused by the 2022 Hunga Tonga-Hunga Ha'pai Volcano eruption on PPP across the Australian region is investigated. It is found that convergence times increased by more than 5 hours across northern Australia due to small-scale ionospheric turbulence. The source of the turbulence was also found in this analysis to be due to a 'super Equatorial Plasma Bubble' that persisted above northern Australia for several hours. This event serves as an excellent example of how ionospheric disturbances can impact relied upon GNSS applications.


## 1 Introduction

At 04:14:45 UT on January 15, 2022, the Hunga Tonga-Hunga Ha'apai Volcano erupted in what was one of the largest explosions on Earth in modern history (Matoza et al., 2022; Wright et al., 2022). It has been estimated that the eruption released somewhere between $3.7 \times 10^{16}$ to $8.37 \times 10^{17}$ Joules (Wright et al., 2022; Astafyeva et al., 2022; Díaz & Rigby, 2022; Vergoz et al., 2022), making it comparable to the Krakatoa eruption in 1883 (Pyle, 2015). The explosion caused a tsunami that reached all sides of the Pacific Ocean with an observed maximum wave-height of 3.4m on the Chilean shoreline (Carvajal et al., 2022). The eruption was even audible as far away as Alaska, which is some 10,000 km away from Tonga (Matoza et al., 2022). Not surprisingly, the eruption caused a myriad of waves in the atmosphere and ionosphere (Themens et al., 2022; Wright et al., 2022; Aa et al., 2022; Astafyeva et al., 2022; Ghent & Crowell, 2022; Maletckii & Astafyeva, 2022; Hong et al., 2022) that were observed to encircle the Earth multiple times (S.-R. Zhang et al., 2022; Matoza et al., 2022; Pradipta et al., 2023).

Waves in the ionosphere can be remotely detected using Global Navigation Satellite System (GNSS) signals in terms of the delay that the ionospheric plasma imparts upon the signals. The phase delay that is measured is related to the total electron content (TEC) between the GNSS satellite and the receiver, with the majority of the TEC contribution coming from the ionosphere (Yizengaw et al., 2008). An expansive network of ground-based GNSS receivers therefore make it possible to geographically map ionospheric TEC around the world (Mannucci et al., 1998) and track the propagation of any ionospheric waves (e.g., Otsuka et al., 2002; Kotake et al., 2006; Borries et al., 2009; Tsugawa et al., 2011; Pradipta et al., 2016; H. Yang et al., 2017; Lay et al., 2018). To date, a range of ionospheric effects associated with the Hunga Tonga Volcano event have been published, and many of these studies have utilized the International GNSS Service network of receivers (Johnston et al., 2017).

Themens et al. (2022) and S.-R. Zhang et al. (2022) reported both large-scale and medium-scale traveling ionospheric disturbances (TIDs) propagating away from the volcano location. S.-R. Zhang et al. (2022) showed evidence of these TIDs continuing to propagate around the world for at least 4 days. Harding et al. (2022) and Le et al. (2022) observed changes to the equatorial electrojet that were caused by variations in the ionospheric dynamo as a result of the eruption. Aa et al. (2022) reported a localized ionospheric plasma depletion in the vicinity of the volcano and increased Equatorial Plasma Bubble (EPB) activity in the Asia-Oceania low-latitude region, which has been further supported by recent modeling efforts (Huba et al., 2022). Evidence of 'super EPBs' has been reported spanning across Chinese (Sun, Wenjie et al., 2022) and Japanese/Australian (Rajesh et al., 2022) longitude sectors following the eruption. Aa et al. (2022) also reported propagating ionospheric irregularities that exhibited a phase speed that matched the prevailing Lamb mode at $\sim$ 315 m/s.

GNSS Precise Point Positioning (PPP) is an advanced positioning technique that uses dual frequency observations made by a single receiver to achieve cm-level positioning accuracy (Zumberge et al., 1997; Leick et al., 2015; Choy et al., 2017; Teunissen & Montenbruck, 2017). Over the previous few decades, the dominant method for achieving cm-level accuracy has been relative positioning, in which a nearby accurately located reference station is used to determine the precise position of a 'rover' receiver (e.g., Odijk, 2002; Hofmann-Wellenhof et al., 2007; Leick et al., 2015; Teunissen & Montenbruck, 2017). Utilizing a nearby reference station makes it possible to eliminate spatially correlated GNSS observations errors, such as the tropospheric and ionospheric delays imposed on the GNSS signals. Unsurprisingly, this precise positioning capability has now found its way into many applications across several major industries, including mining, agriculture and construction (e.g., Pérez-Ruiz et al., 2015; Choy et al., 2017; Woodgate et al., 2017; Rao et al., 2022). Over recent years, PPP is fast becoming the new global standard for cm-level positioning applications due to its ability to model and account for GNSS observations errors without the need for a nearby reference station. However, the most significant drawback that is limiting the widespread uptake of PPP is the rather long convergence times, which are typically on the order of 10s of mins to hours (Bisnath & Gao, 2009; Van Bree et al., 2009; Choy et al., 2017). As a result, researchers have been investigating methods to significantly reduce PPP convergence times (e.g., Collins & Bisnath, 2011; Collins et al., 2012; Geng & Bock, 2013; H. Zhang et al., 2013; Banville et al., 2014; Li et al., 2015; Duong, 2020). Given the significant influence of the ionosphere on GNSS signals, space weather poses a potential vulnerability to the PPP technique and its anticipated widespread up-take. As such, researchers have also been investigating the impact of solar and geomagnetic activity on PPP (e.g., Luo et al., 2018; Poniatowski & Nykiel, 2020; Z. Yang et al., 2020; Zha et al., 2021; Luo et al., 2022).

The Hunga Tonga Volcano eruption provides a unique opportunity to uncover new fundamental knowledge of the physics of atmosphere-ionosphere coupling. In addition, given the adverse influence of ionospheric variability on GNSS, this event can also pro-


Figure 1: The locations of the ionosondes used in this analysis. Tonga is indicated by the red cross.

vide insights into the impact of such ionospheric disturbances across broader society, particularly in industries that rely heavily on precise GNSS positioning. In this study, the impact of the Tonga volcano eruption on Global Positioning System (GPS) PPP across the Australian region is explored. Supporting this analysis are the data collected by ionosondes throughout the region that show both TID and Spread-F activity in the wake of the volcano eruption. The PPP accuracy throughout the day of the eruption is explored, followed by an analysis of the PPP convergence times from stations located throughout the region. Finally, ionospheric observations using GPS receivers across the region are used to investigate the physical mechanisms causing the disruptions identified in this study.

## 2 Data

In this analysis, the Australian Bureau of Meteorology Space Weather Services' ionosonde data are used. Figure 1 shows the locations of the ionosonde stations (black triangles) and Tonga volcano (red cross). The stations are Niue (NUE5F; 19.07°S, 190.07°E), Norfolk Island (NLK5D; 29.03°S, 167.97°E), Canberra (CBR5F; 35.32°S, 149.00°E), Townsville (TVL5F; 19.63°S, 146.8°E), Darwin (DWN5D; 12.45°S, 130.95°E), Perth (PER5D; 31.94°S, 115.95°E), Learmonth (LEA5D; 22.25°S, 114.08°E) and Cocos Keeling Islands (CCK5F; 12.20°S, 96.80°E). Each ionosonde generates ionograms by sweeping through radio frequencies between 2-22 MHz, transmitting and receiving ionospheric echoes that indicate the electron density for a given virtual height determined by time-of-flight. In this analysis, the ionosonde data were used to indicate the presence of TIDs and spread-F traces.

The ionosonde data complement the primary dataset used in this study, namely the GPS receiver data. GPS Continuously Operating Reference Station (CORS) data from stations located across Australia, spanning into the Southeast Asian region and across the South Pacific, were used in this analysis. While previous works have employed such GPS CORS data to analyze ionospheric TEC fluctuations caused by the eruption, this study focuses on the impact of this eruption on the GPS application of PPP.

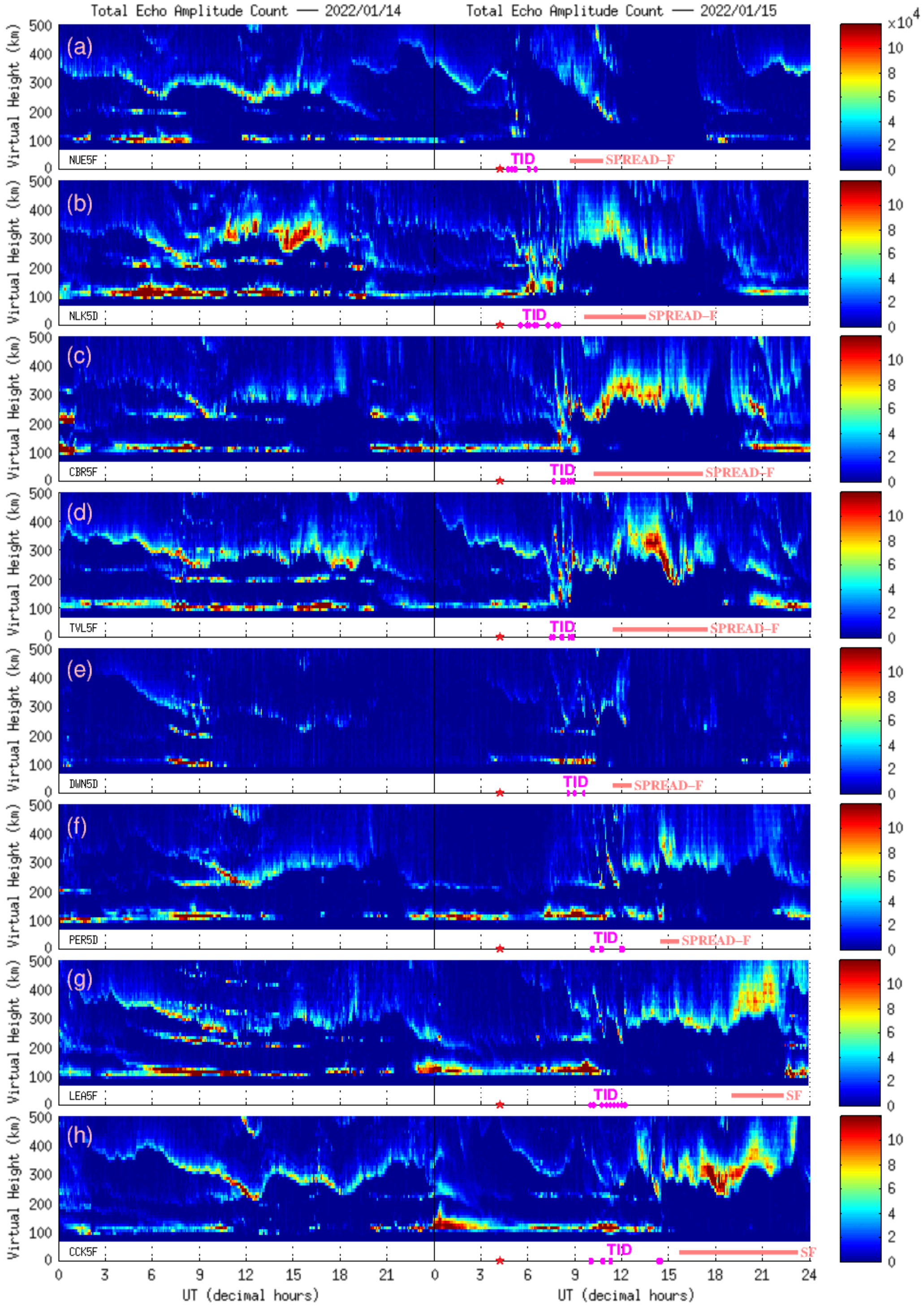


Figure 2: Range-time-intensity-style plots of ionospheric echoes received from ionosondes across the Australian region during January 14-15, 2022. Each panel corresponds to each station; (a) Niue (NUE5F), (b) Norfolk Island (NLK5D), (c) Canberra (CBR5F), (d) Townsville (TVL5F), (e) Darwin (DWN5D), (f) Perth (PER5D), (g) Learmonth (LEA5D) and (h) Cocos Keeling Islands (CCK5F). The color of each bin indicates the number of echoes received in that virtual height bin across all scanning frequencies, as indicated in the color bar on the right. The red stars indicate the time of the eruption; 04:14:45 UT. The pink dots (salmon bars) indicate the presences of TID (Spread-F) signatures.

The Geoscience Australia's Ginan system was used for performing the PPP calculations[1]. PPP is a high accuracy positioning method used to correct errors in GNSS positioning based on the robust modelling and estimations of systematic errors in the GNSS signals. The specific Ginan setup used in this analysis closely follows the Ginan PPP example "Ex11", in which the PPP is performed in 'static mode' using the ionosphere-free combination[2].

The carrier-phase measurements between the GPS satellites and receivers were used to calculate the TEC along the signal path (i.e., the slant TEC, sTEC) following similar methodology to Le Huy et al. (2016) and T. Dao et al. (2020). The possible jumps in the sTEC values estimated from the carrier-phase measurements due to cycle slips were eliminated by comparing them against the sTEC estimated from the pseudo-range measurements that were smoothed by a fourth-degree polynomial approximation. A difference between the carrier-phase sTEC and the pseudo-range sTEC of more than 5 TECU was taken to indicate an instrumental data jump/spike in the carrier-phase sTEC; in such instances, the smoothed pseudo-range sTEC was used. The sTEC was then compared with the Centre of Orbit Determination in Europe Global model to determine the total delay of device (including biases), using elevation angles above 30° to remove multipath effects. Finally, the resulting sTEC was converted to the vertical total electron content (VTEC) observed at the pierce point of the ionosphere by using a single-layer model (Klobuchar, 1986) and an assumed altitude of 400 km.The presence of scintillation-causing small-scale ionospheric irregularities can be detected using the rate of TEC index (ROTI), which is defined as the 5-min standard deviation in the rate of change in the sTEC for each satellite-to-ground link (Pi et al., 1997).

## 3 Results

This analysis begins with an overview of the ionospheric conditions before and after the arrival of the disturbances caused by the volcano eruption using the ionosonde network in Fig. 1. First, it is worth mentioning that a minor geomagnetic storm occurred in the late hours of January 14, with Dst reaching -91 nT due to a small, short-lived recurrent solar wind stream that had a minimal effect on the equatorial electric field (Le et al., 2022). A useful way to analyze temporal changes in ionograms is by representing the data in a format similar to a 'range-time-intensity' plot (Pradipta et al., 2015; Carter et al., 2018; Currie et al., 2021). Instead of using total power, Pradipta et al. (2015) integrated over the dBm amplitudes across all sounding frequencies, effectively creating a sum of digitized echoes. This methodology was adopted for the present study. Figure 2 shows these range-time-intensity-style plots for the ionosondes during January 14-15, 2022; the panels are ordered by the station great circle distance to Tonga, closest to farthest. The colors indicate the number of echoes received across all frequencies in each virtual height bin (10 kms). The presence of TIDs and spread-F traces are indicated at the bottom of each plot by the pink dots and salmon bars, respectively; these have been determined by visual inspection of the ionograms.

Figure 2 shows a range of ionospheric conditions across January 14 and 15; e.g., sporadic E features at virtual heights of 100 km are present for all stations at various times and F region traces that display typical altitude changes with time. TID signatures are also clear in the data on January 15 for all stations, beginning at approx. 4:30 UT at Niue (top panel) and at approx. 10 UT at Cocos Keeling Islands, with the other stations showing the TID signatures at times in between. All stations, with the exception of Darwin which was suffering some intermittent hardware issues during this period, show the presence of spread-F traces in the hours following the TIDs, and in all cases,

[1] https://geoscienceaustralia.github.io/ginan/
[2] https://geoscienceaustralia.github.io/ginan/codeDocs/Pea_8Configuration_8Examples.html

the spread-F traces are persistent for a number of hours. In particular, the TID activity at Norfolk Island begins shortly before 6 UT, with Spread-F present from 09:15 UT until 13:30 UT. Thus, the occurrence of spread-F traces measured by the Norfolk Island ionosonde span local times (LT) 21:15-01:30. At Townsville, the TIDs are first observed close to 7 UT (17 LT) and bring with them batches of Spread-F. The Spread-F then intensifies close to 11:24 UT (21:24 LT) and remains strong until 15 UT (1:00 LT), before finally ceasing at 17:30 UT (03:30 LT).

Next, the GPS data from receivers close to the Norfolk Island and Townsville ionosonde stations are examined as initial examples of the features and trends present throughout the GPS data. Figure 3 shows the observed vertical TEC (VTEC, upper panels) and the rate of TEC index (ROTI, lower panels) observed by the Norfolk Island (NORF, left) and Townsville (TOW2, right) GPS receivers on January 15, 2022. The VTEC data for both stations show the presence of TIDs that disrupt the diurnal pattern starting at $\sim$ 6 and 7 UT for NORF and TOW2, respectively, in good agreement with the ionosonde observations in Fig. 2. In the NORF data, the TIDs are observed in the individual satellite traces as rather small-amplitude wave structures compared to the variations over the 24-hour period. Slight differences in the timings of these structures (or phase progression) for different satellite links are due to the geographical spread of the ionospheric pierce points and the motion of the TIDs over the station. In the TOW2 data, the TIDs are much clearer as strong changes in VTEC for specific satellite links at different times. The phase progression of the VTEC structures overhead are much clearer in the TOW2 data. The lower panels reveal the times in which increased ROTI values were observed. For Norfolk Island (Fig. 3c) ROTI increases shortly after the TIDs arrive and then decreases back to low levels by 9 UT. Townsville also observed increased ROTI values once the main TIDs arrived and remained high until $\sim$ 15 UT once the strong Spread-F ceases, c.f. Fig. 2.

Next, we illustrate how the Ginan PPP software achieves convergence, as defined here by a 3-D position error of less than 10 cm. Figure 4 shows six examples of PPP convergence on January 15, 2022 using data collected by the NORF (top row) and TOW2 (bottom row) receivers. Each panel represents a ‘cold start’ of the PPP algorithm starting at a different time; 02:30 UT, 04:30 UT and 06:30 UT, as indicated in the subfigure titles. The positioning error was calculated as the difference between the PPP estimations and the known geodetic station locations. The position errors in the X, Y, and Z directions, as well as the full 3-D position, are shown in each panel. The 10 cm position error threshold is indicated by the dash-dot line, and zero error is indicated by the dashed line. Also displayed in each panel is the time it took for the 3-D position error to reach below 10 cm, indicated by the vertical dotted line; i.e., the convergence time.

Given the TID and subsequent Spread-F activity shown in the ionosonde data in Fig. 2, one might expect that PPP errors for nearby GPS receivers would noticeably increase during these periods. However, Fig. 4a shows that despite the onset of TIDs at approx. 6 UT for the NORF station, the position error remained below the 10-cm threshold. The same is true in Fig. 4d for the TOW2 station, for which the onset of TIDs was approx. 7 UT. While Fig. 4b shows that the NORF station position error increased following the commencement of Spread-F close to 9 UT, it remained well below 10 cm. Interestingly, despite the commencement of rather strong Spread-F at 11:24 UT at TOW2, Fig. 4f shows no significant increase in the position error. This is likely the result of running the PPP algorithm in ‘static mode’. From these results, one can conclude that the static-mode PPP algorithm was robust enough to remain at cm-level accuracy for these stations throughout the turbulent ionospheric conditions caused by the Tonga eruption, provided that convergence had already been achieved.

Figure 4 also illustrates how the convergence time is dependent on the start time of the algorithm. For the NORF station, the convergence time ranges from less than 1 hour beginning at 04:30 UT (Fig. 4b) to almost 4 hours when started from 06:30 UT (Fig.

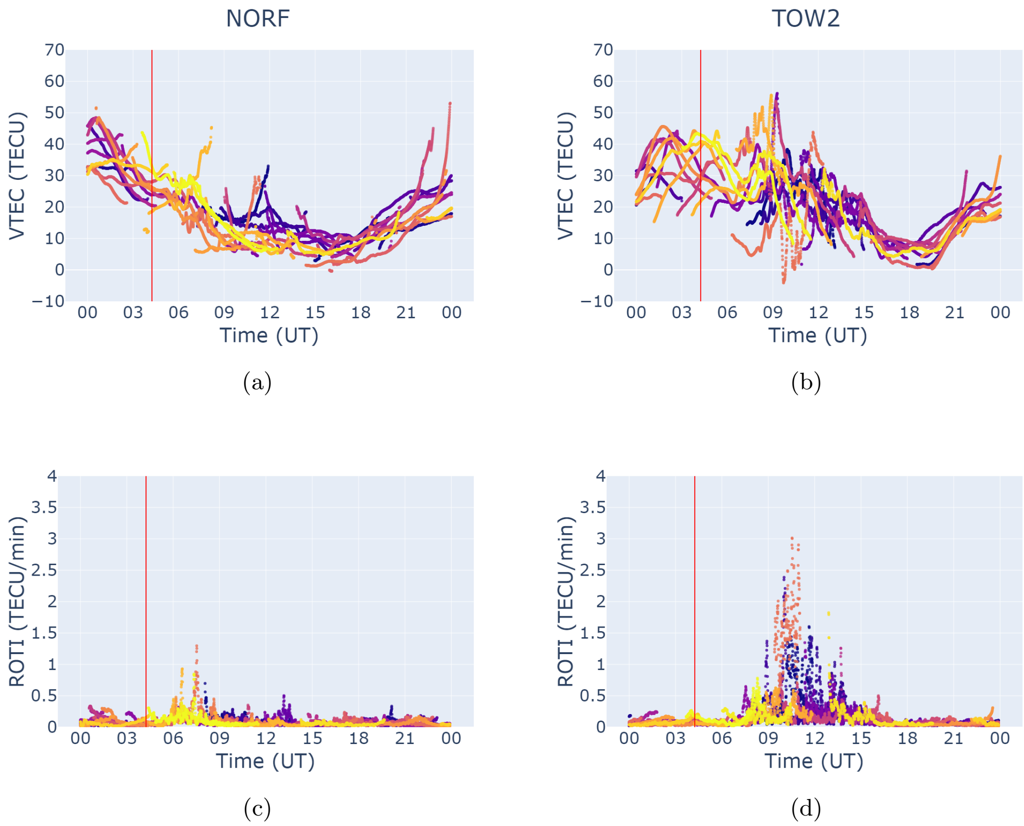


Figure 3: VTEC measured by (a) Norfolk Is. (NORF) and (b) Townsville (TOW2) GPS receivers with the different colors representing different satellite-to-ground links on January 15, 2022. The corresponding ROTI values for (c) NORF and (d) TOW2 stations. The red vertical lines indicate the time of the eruption.

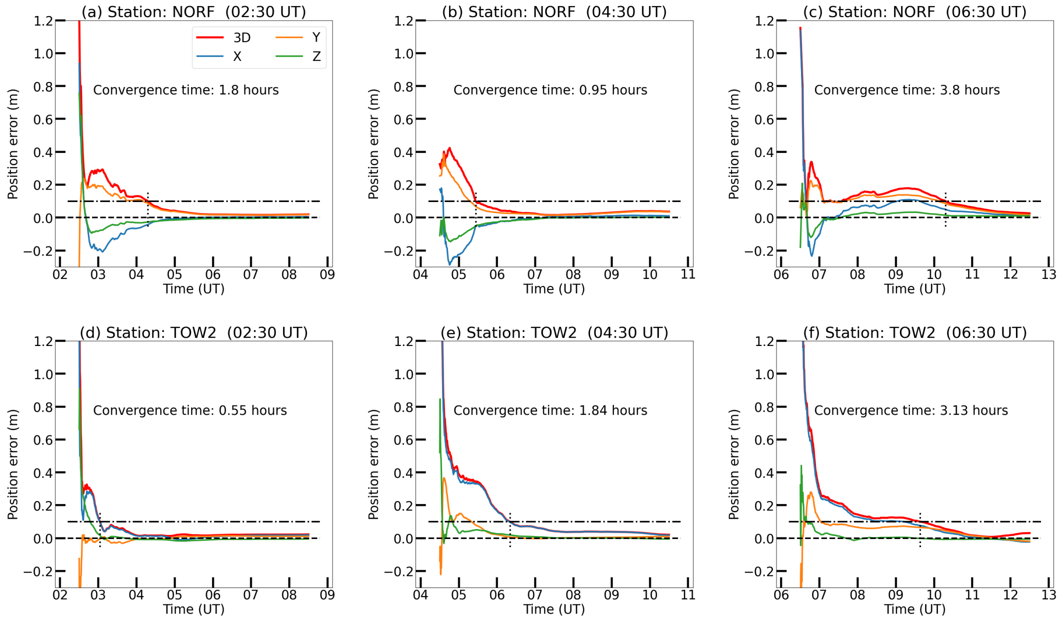


Figure 4: Examples of PPP convergence from a cold start using GPS data from the NORF (top row) and TOW2 (bottom row) commencing at 02:30 UT (left column), 04:30 UT (centre column) and 06:30 UT (right column) on January 15, 2022. Shown in each panel is the positioning error in X, Y and Z coordinates, in addition to the full 3-D position error. The dashed and dot-dashed horizon lines indicate position errors of 0 m and 10 cm, respectively. The moment when convergence was achieved and the associated convergence time are indicated in each panel by the vertical dotted lines and the text, respectively.

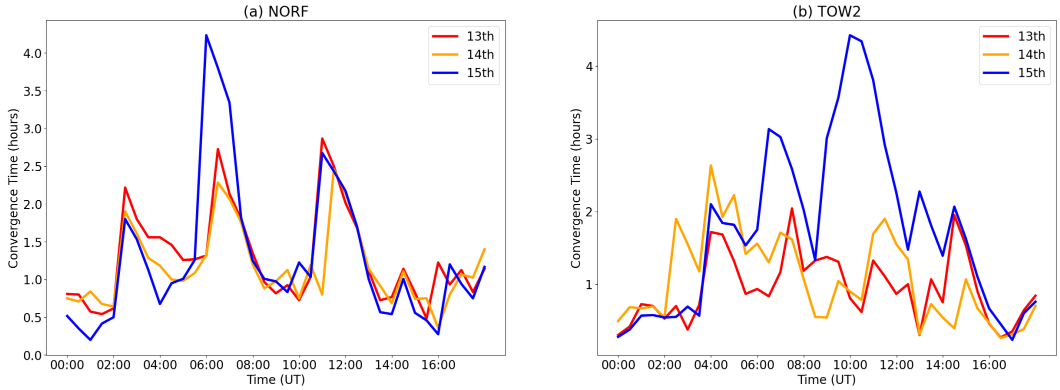


Figure 5: Diurnal variations in the PPP convergence time for the (a) NORF and (b) TOW2 GPS stations on the 13th, 14th and 15th of January, 2022.

4c). The TOW2 station shows a similar level of variation, ranging from 30 mins when started from 02:30 UT (Fig. 4d) up to more than 3 hours when started from 06:30 UT (Fig. 4c), which is ∼ 30 mins before the eruption effects reached Townsville. These results suggest a possible connection between the variable ionosphere in the wake of the eruption and the PPP convergence times at Norfolk Island and Townsville.

The PPP convergence time is a complicated parameter that is dependent on the number and geometry of available satellites, and the ability of the algorithm to model and account for the signal errors including the atmospheric components caused by the ionosphere and troposphere (e.g., Zumberge et al., 1997; Leick et al., 2015; Choy et al., 2017; Kouba et al., 2017; Teunissen & Montenbruck, 2017). To further explore the possible impact of the disturbed ionosphere on the PPP convergence time, a numerical experiment was performed using the GPS CORS across the Australian region. The Ginan software was used to perform the PPP processing using data from staggered start times throughout January 13-15, 2022, in 30-min steps. In other words, the experiment simulated a series of 'cold starts' of the PPP algorithm every 30-mins during January 13-15, 2022. At each time and for each station, the time it took for the PPP algorithm to achieve convergence was recorded. Figure 5 shows how the convergence time for the NORF (a) and TOW2 (b) stations varied throughout January 13-15. For January 13 and 14, convergence times for both stations were typically on the order of 30 mins to 2.5 hours, and appear to follow a similar diurnal variation for each station. On January 15, however, the convergence times are typically 2-4.5 hours, with some times showing significant differences compared to the January 13 and 14 values; particularly close to 6 UT for NORF and between 6 and 12 UT for TOW2. For NORF, the maximum increase in convergence time on January 15 (relative to January 14) was almost 3 hours at 6 UT. For TOW2, the maximum increase in convergence time was 3.6 hours at 10:30 UT.

In order to investigate what impact, if any, the disturbed ionosphere had on GPS PPP convergence time across the region, a reliable baseline was needed. At first glance of Fig. 5, it appears that simply choosing the PPP convergence time from the day prior as the baseline is a good option. However, some GPS stations showed significant differences between the diurnal variations in the convergence times between January 13 and 14; not shown here. In these cases, it is possible that the differences could be explained by a difference in the handling of the tropospheric delays by the algorithm, as the geomagnetic activity level was quiet and the satellite geometry was very similar. Therefore, in order to exclude times and GPS stations' data for which the chosen baseline of January 14 was not reliable, a simple selection criterion was used. Namely, if the con-

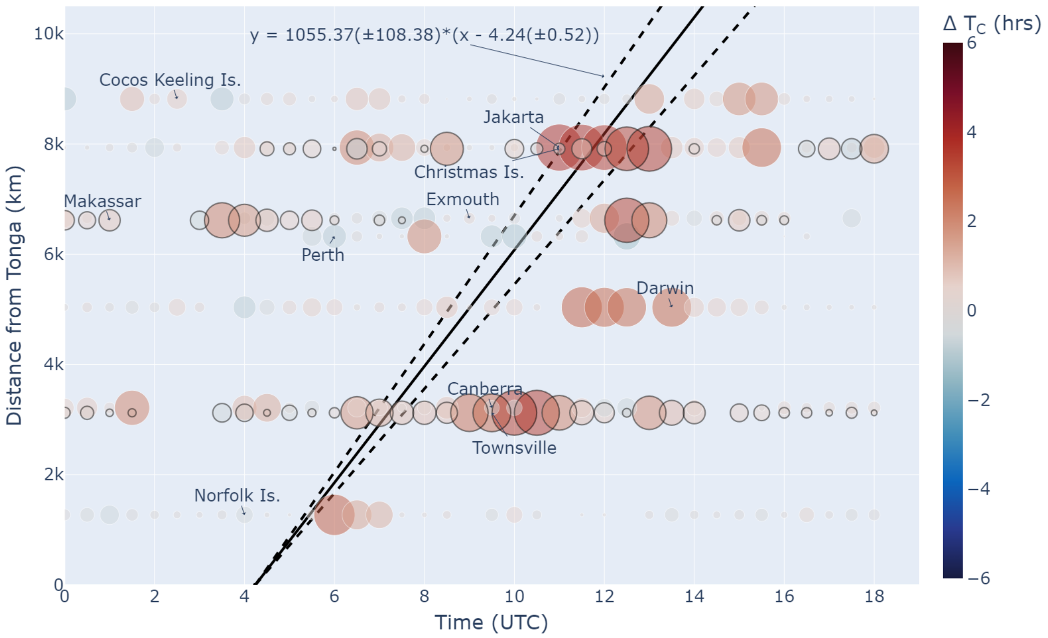


Figure 6: Distance from Tonga versus time colored according to the change in PPP convergence time, $\Delta T_C$, as determined using GPS stations located near the ionosonde stations in Figure 1, and two additional stations located at Makassar and Jakarta. The size of the circles also indicates the $\Delta T_C$ value. For reference, the trend line representing the propagation of the ionospheric disturbances as identified in the ionosonde data in Fig. 2 is shown. Due to some stations' data overlapping in the plot, Townsville, Makassar and Christmas Island data points are shown with black outlines.

vergence time for a given moment in the day of January 14 was different compared to January 13 by more than 1 hour, then that time was considered as a 'null' data point. Otherwise, the difference between the convergence time on January 15 and January 14 for that time of day was taken as the change in convergence time due to the disturbed ionosphere on the day of the Tonga volcano eruption, $\Delta T_C$.

Figure 6 shows how the change in convergence time varied throughout January 15 for GPS stations colocated with the ionosondes in Fig. 1, with two additional stations at farther distances; Makassar and Jakata in Indonesia. The size and color of the dots indicates the change in convergence time, $\Delta T_C$. Also plotted is the line of best fit that describes the propagation of the TIDs as detected by the ionosondes from Pradipta et al. (2023).

Firstly, it is worth mentioning that prior to the arrival of the TIDs, some GPS stations in Fig. 6 show some isolated increases in the convergence time on January 15 compared to January 14. Makassar, Christmas Island, Canberra and Perth all show isolated increases in the convergence time on the order of 2 hours before any ionospheric disturbances from the eruption arrive. However, most of the stations in Fig. 6 show significant and lasting convergence time increases after the TIDs arrive at their respective locations. There are the exceptions of Canberra, Exmouth and Perth that do not observe any clear convergence time increases. Interestingly, some GPS stations show convergence time increases the moment the TIDs arrive, for example Norfolk Island and Jakarta, whereas others observe their largest increases some hours later, for instance Darwin and Townsville.

In the Townsville ionosonde data shown in Fig. 2, it was noted that spread-F traces accompanied the arrival of TIDs at 7 UT (17 LT), with strong spread-F traces observed during 11:24-15:00 UT (21:15-01:00 LT). It is interesting to note that the largest $\Delta T_C$ increases for the TOW2/Townsville GPS station occurred for the algorithm start time of 10:30 UT (20:30 LT), consistent with the beginning of the 3.5-hour period of strong Spread-F activity detected by the Townsville ionosonde. Finally, it is also worth noting that the magnitude of the $\Delta T_C$ increases vary between the stations, from an increase of 2 hours observed at the Cocos Keeling Islands to an increase of 3.6 hours observed at Townsville and 3.8 hours at Jakarta.

To further explore the impact of the disturbed ionosphere on the GPS PPP convergence time across the region, Fig. 7 shows $\Delta T_C$ for all of the GPS stations each hour between 6 UT and 15 UT on January 15. At 6 and 7 UT, it can be seen that $\Delta T_C$ values were mostly close to 0; some stations across South Eastern Australia show some elevated values at 6 UT, but most reduce to 0 by 7 UT. At 6 UT, the Norfolk Island station – located to the southwest of Tonga approximately halfway to Australia – is already showing elevated convergence times, as also shown in Fig. 6. By 8 UT, some stations on Australia's northeastern coast are showing some elevated convergence times, which further increase at 9 UT. At this time, several stations show convergence time increases of more than 5 hours. At 10 UT, the convergence time increases in the far-north Australian region begin to decline as stations further south begin to show increases that reach 4 hours for some stations. The $\Delta T_C$ values are still elevated at 11 UT in the east Australian region, but some stations farther north and to the west are showing values close to 5 hours. At 12 UT, the elevated $\Delta T_C$ values across Australia's north and across Southeast Asia remain at 3-4 hours as the eastern Australian stations approach 0. There is a slight increase in $\Delta T_C$ across Australia's northeast once again at 13 UT to more than 3 hours, before almost all stations across the region approach $\Delta T_C = 0$ by 15 UT. An interactive map showing these data is included in the Supplementary Materials (S1).

In an effort to diagnose the physical phenomena that may be responsible for these impacts on PPP convergence, ionospheric observations made by these GPS stations are examined next. Figure 8 is the similar to Fig. 6, but the data points are colored according to the maximum ROTI value detected for each GPS station in each 30-min interval. Similar to the increased convergence times in Fig. 6, the ROTI values for most stations show a marked increase following the arrival of the TIDs from the volcano. Some stations observed increased ROTI values some time after the primary TID arrivals, such as Norfolk Island, Townsville and Darwin. The Perth and Exmouth stations generally show very low ROTI values, as does the Canberra station; although at 08:30 UT, Canberra shows one elevated ROTI value. The agreement between the ROTI results in Fig. 8 and the convergence time results in Fig. 6 suggests a strong link between the two.

To explore the potential link between ROTI and PPP convergence time, Figure 9 is similar to Fig. 7 but shows the 30-min maximum ROTI value for each GPS receiver; the full interactive map is available in the Supplementary Materials (S2). These maps show a lot of similar trends to those in Fig. 7, particularly the increased ROTI values over the northern Australian region compared to the south, and the increased values going into the Southeast Asian region. However, there is one notable difference between Figs. 7 and 9; namely panel (d) that corresponds to 9 UT. While the change in convergence times were low throughout South Eastern Australia, the ROTI values in Fig. 9 show that ROTI was actually quite high across this region. While the wave of increased ROTI clearly sweeps across northern Australia, the increased ROTI across southern parts of the country disappeared in place and did not make it to Western Australia.

Finally, VTEC observations made by the GPS stations are presented. Figure 10 is a series of maps of the 15-min averaged VTEC (i.e., $\langle VTEC \rangle$) for a select group of GPS stations at latitudes between 24°S and 10°S and longitudes between 128°E and 152°E (geographic). Each point represents the ionospheric pierce point (IPP) assuming an al-

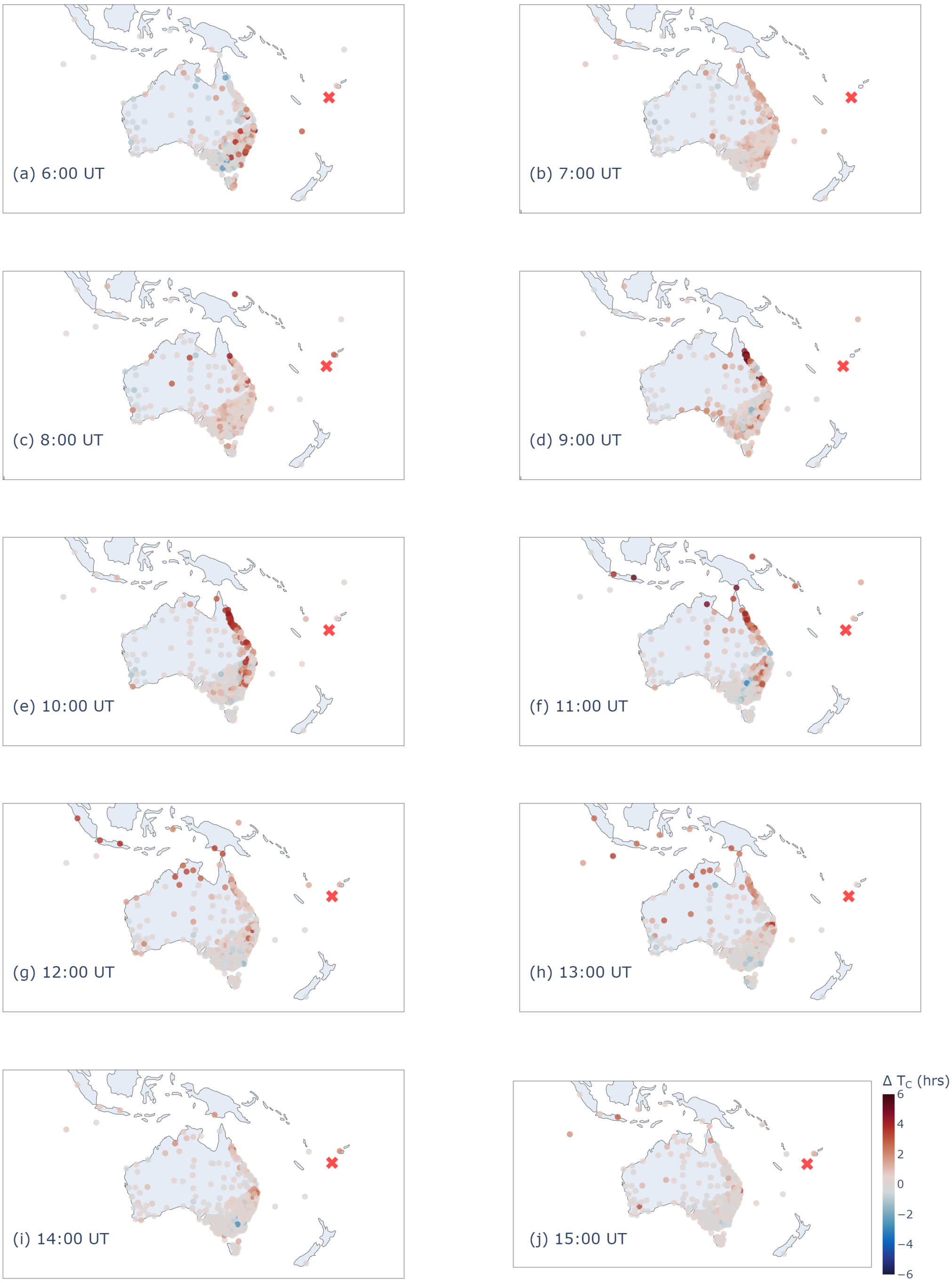


Figure 7: The change in PPP convergence time for GPS stations across the Australian/Southeast Asian region from (a) 6 UT until (j) 15 UT. The red cross indicates the location of Tonga. The full interactive map is included in the Supplementary Material S1.

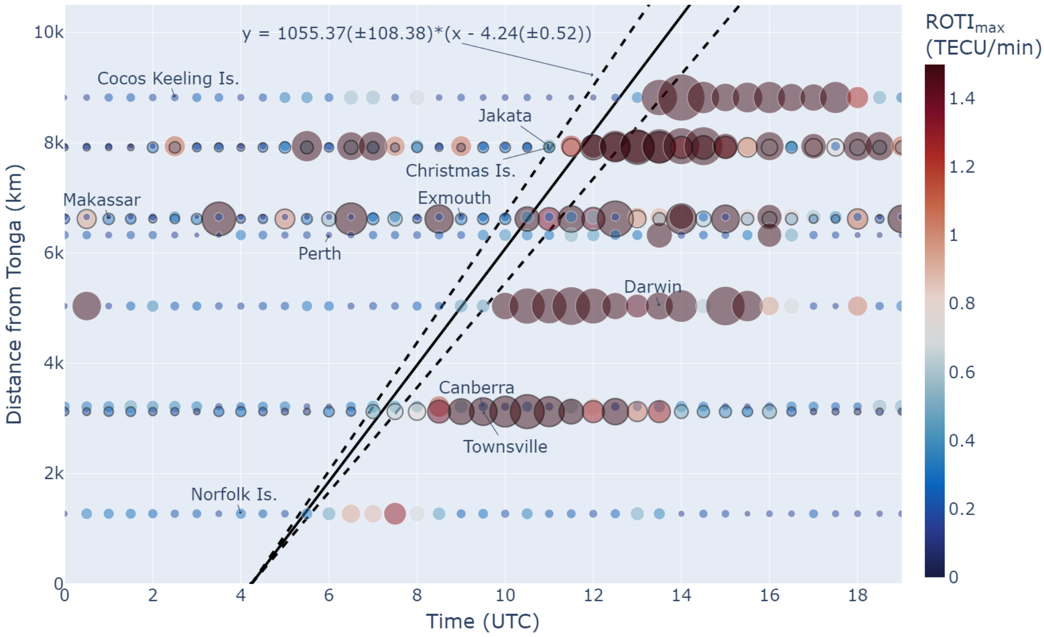


Figure 8: Same as Fig. 6, but colored according to the maximum ROTI observed for each station in every 30-min interval. Once again, Townsville, Makassar and Christmas Island data points are shown with black outlines.

titude of 400 km. A full interactive animation of this data sequence is included in the Supplementary Materials (S3). Figure 10a shows the presence of a deep $\langle VTEC \rangle$ valley over eastern of Papua New Guinea at 9 UT. By 09:30 UT (Fig. 10b) it appears as though the $\langle VTEC \rangle$ valley/depletion extends south to the Townsville station, and remains almost in place for the remaining times plotted. The shape of the $\langle VTEC \rangle$ depletion is quite pronounced in Fig. 10e (11 UT) as a thin dark blue feature with a north-south alignment. Within this depletion, values as low as 6 TECU were observed, and were as high as 48 TECU only 300 km to the west.

To track and measure the propagation of this $\langle VTEC \rangle$ depletion feature, Figure. 11 shows the same data from Fig. 10, but it is restricted to spanning latitudes 17°S–14°S and longitudes 140°E–155°E; i.e., the blue box in 10c. The depletion noted in Fig. 10 is quite clear in Fig. 11, along with some other $\langle VTEC \rangle$ variations during this interval. Fig. 11 also includes a manually plotted trendline that highlights the propagation of the most pronounced depletion with longitude; $y = 0.942x + 135.78$. A noteworthy observation is that this ionospheric depletion is propagating to the east, albeit rather slowly. As the trendline indicates, the depletion is propagating eastwards with a speed of $\sim 0.9$ °/h, or equivalently $\sim 30$ m/s (assuming 111 km/°).

## 4 Discussion

In the results above, the ionospheric variability resulting from the Hunga Tonga Volcano eruption across the Australian region was presented, followed by an investigation of the associated impact on PPP accuracy and convergence time. It was found that positioning accuracy did not appear to be adversely impacted in the wake of the eruption. Although, an experiment simulating 'cold starts' to the PPP algorithm showed that convergence times were affected by the variable ionosphere in the wake of the eruption.

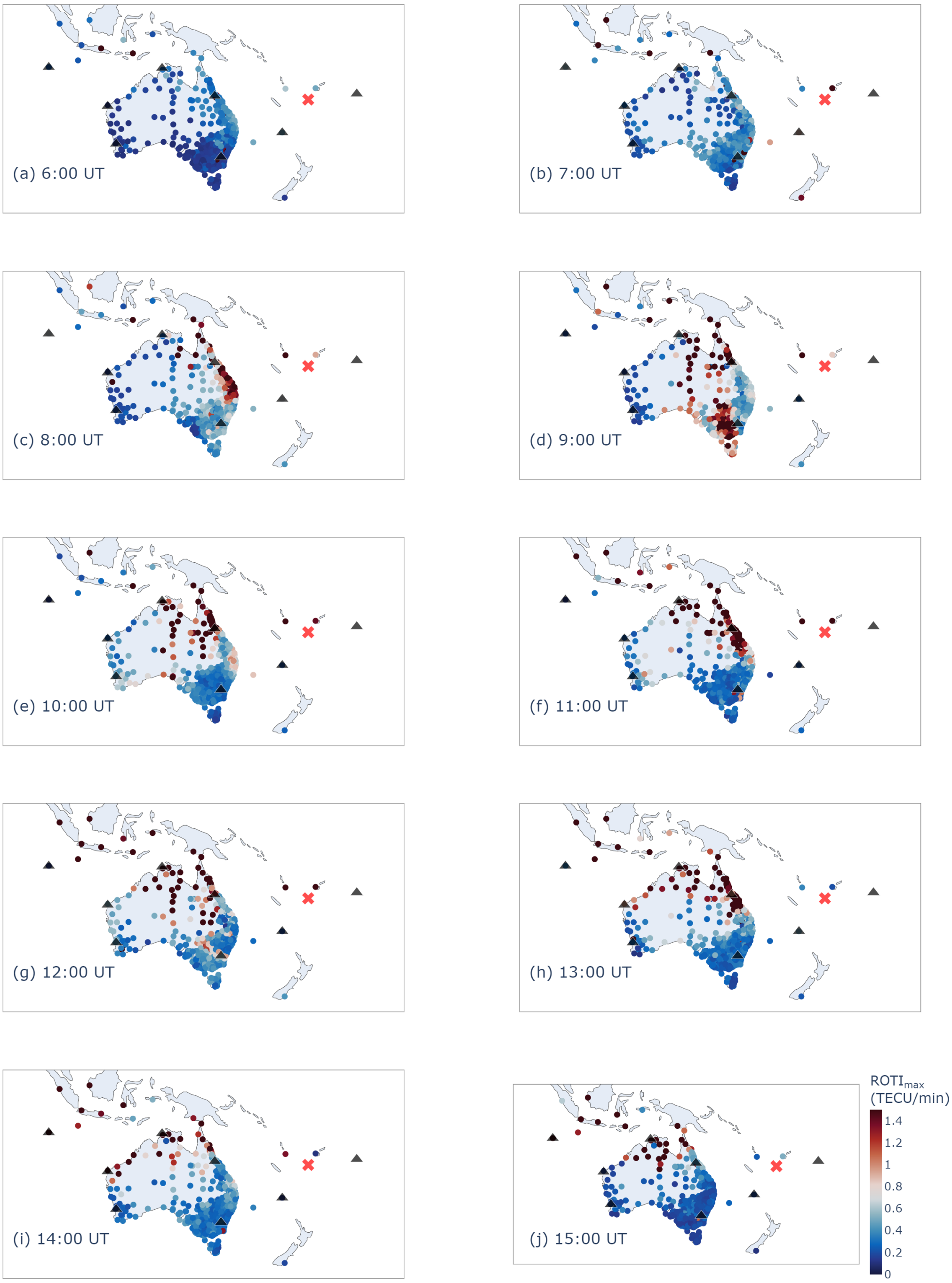


Figure 9: Same as Fig. 7, but showing the observed ROTI maximum in the 30-min following each time; i.e., panel a displays the maximum ROTI observed by each station between 6 and 6:30 UT. The full interactive map is included in the Supplementary Material S2.

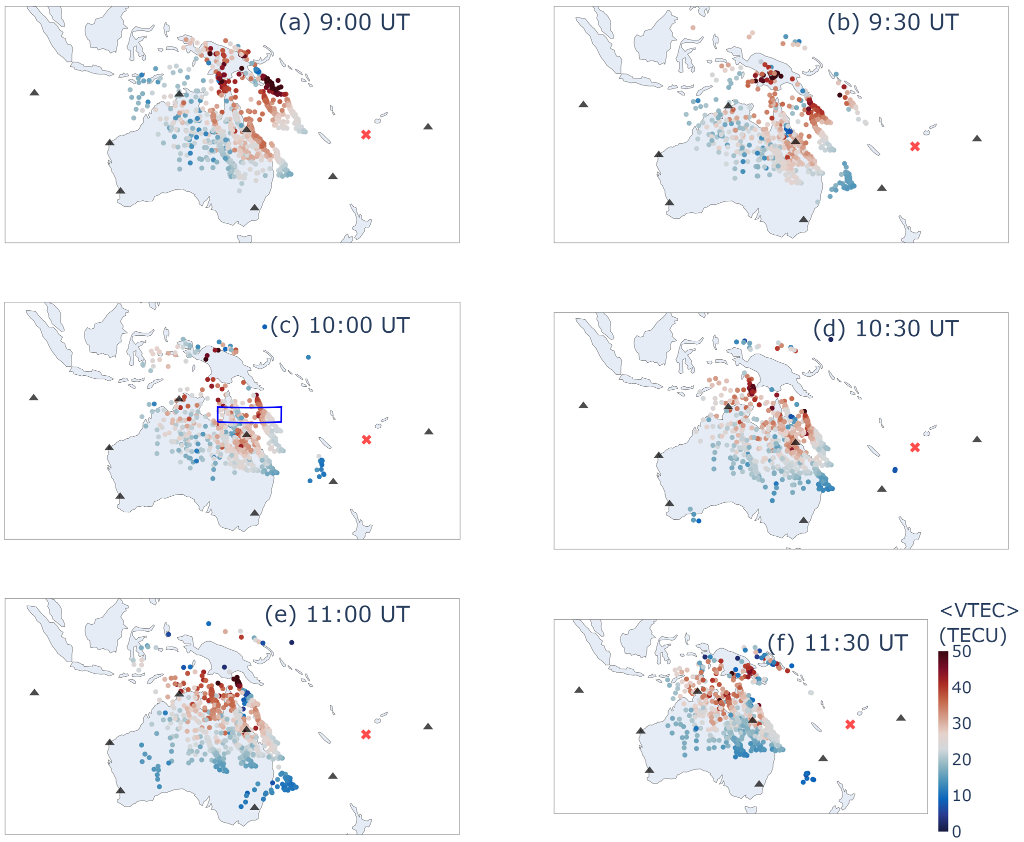


Figure 10: Maps showing the 15-min averaged VTEC (i.e., $\langle VTEC \rangle$) from 9 UT to 11:30 UT on January 15, 2022 for stations located between latitudes 24°S and 10°S and longitudes 128°E and 152°E (geographic). The blue box in panel (c) shows the range of latitudes and longitudes considered in the analysis to follow. The full interactive map is included in the Supplementary Material S3.

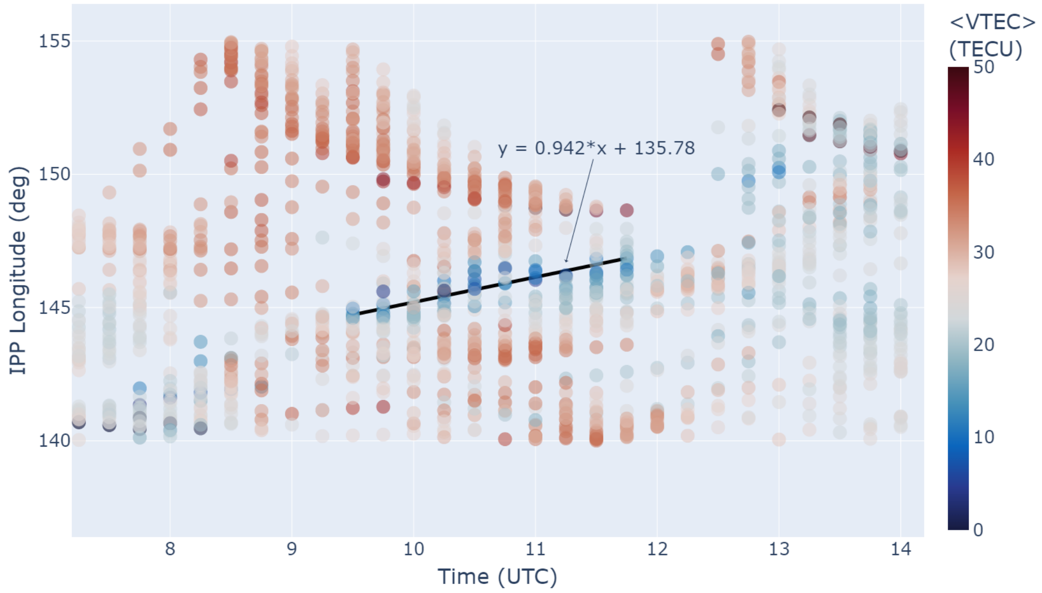


Figure 11: Ionospheric pierce point longitude versus time for data points for locations within the blue box in Fig. 10c – latitudes 17°S–14°S and longitudes 140°E–155°E – colored according to $\langle VTEC \rangle$.

Using the PPP convergence times from 13 and 14 January as a baseline, it was found that stations across northern Australia and Southeast Asia experienced significant convergence time increases on January 15, with some stations experiencing increases of more than 5 hours. It was revealed that the stations experiencing the largest convergence time increases measured extended periods of enhanced ROTI values. Examination of the 15-min averaged VTEC data then revealed the presence of a significant depletion that extended from Papua New Guinea into central eastern Queensland. A close examination of this depletion revealed that it was propagating eastwards with a velocity of $\sim 30$ m/s.

PPP accuracy is at the core of PPP as a usable application. As such, previous works that have studied the impact of adverse ionospheric conditions on positioning focus on the solution accuracy, and this has typically been done using 'kinematic' mode. For instance, Poniatowski and Nykiel (2020) reported the degradation of PPP accuracy across central Europe during the 2015 St. Patrick's Day storm, with root mean square errors of 0.58m, 0.37m and 0.26m in the vertical, north and east directions, respectively. Z. Yang et al. (2020) also investigated the impact of the 2015 St. Patrick's Day storm on PPP accuracy, but their analysis included stations located around the world. They found that intense auroral activity played a significant role in degrading the PPP solutions, with $\sim 70\%$ of high-latitude stations suffering position errors of greater than 1 m. Importantly, the most severe degradations in position accuracy were found to coincide with intense ionospheric irregularities, as determined by the GPS ROTI parameter. Z. Yang et al. (2020) also attributed some observed position accuracy degradation in low latitudes to large-scale TIDs – $\sim 1$ TECU in amplitude – that were generated by the storm. In the present study, the PPP errors during the passage of the TIDs from the volcano eruption – and the subsequent Spread-F activity – appeared to be smaller compared to that reported by Z. Yang et al. (2020), despite the larger amplitude of the initial TIDs for this event, $\sim 3$ TECU (S.-R. Zhang et al., 2022). A similar analysis of the 2017 September geomagnetic storms also revealed a strong relationship between enhanced ROTI and de-graded PPP accuracy (Zakharenkova & Cherniak, 2021). In their analysis, it was found that the 3-D errors rose to several meters due to the presence of small-scale ionospheric irregularities. The lower errors in the present study can be understood by the fact that 'static mode' was used in the positioning algorithm; i.e., the range of potential receiver velocities passed to the filter via the 'process noise' parameter was set to zero. Interestingly, the positioning errors in this study remained lower than 10 cm, provided that the solution had already converged. One exception is shown in Fig. 5c, where the arrival of TIDs at NORF delayed the convergence by $\sim 2$ hours. While Figure 5 only shows a few examples for two stations, their results largely reflect the results of the other stations considered in this analysis. Given the rather minimal impact of the volcano eruption on static-mode PPP accuracy across the Australian region, the focus of this study shifted to the potential impact on the PPP convergence time, which is a key limiting factor in the widespread use of PPP (Choy et al., 2017).

Here, the investigation into the PPP convergence time made use of an experiment in which 'cold starts' to the positioning algorithm were performed every 30-min during January 15, 2022. Perhaps the most significant finding in this study is that the change in convergence time – i.e., the difference between the 15th and 14th – reached 5 hours or higher for some stations. Interestingly, these convergence time increases were consistently observed over northern Australia, and were largely absent across central and southern Australia, c.f. Figs. 6 and 7.

At first glance, the ionosonde data showed several inconsistencies with the PPP convergence time results. All ionosonde stations observed clear TIDs associated with the volcano eruption, followed by some period of Spread-F activity in the ionograms. As reported by Pradipta et al. (2023), the propagation of the disturbances in these ionosonde data agrees well with other studies that have investigated the TID propagation using GPS TEC data (e.g., Themens et al., 2022; S.-R. Zhang et al., 2022). As observed by most ionosonde stations, the TIDs immediately gave way to Spread-F activity, but in some cases there was a significant delay between the arrival of the TIDs and the onset of Spread-F. For example, the Townsville station TVL5F, Fig. 2d, showed Spread-F activity commencing some 3 hrs after the initial TIDs passed, and the Learmonth station showed Spread-F commencing more than 6 hours after the TID passage. The intensity of the Spread-F also widely varied across the stations. Stations like Canberra, Townsville and Cocos Keeling Islands observed quite strong and prolonged Spread-F, whereas one of the stations closest to the eruption, Norfolk Island, and another among the farthest away, Perth, observed relatively weak Spread-F activity.

To better understand the differences in the detection of Spread-F across the Australian region, it helps to be reminded about what the presence of TID signatures and Spread-F in the ionograms indicates about the ionospheric plasma. The TID signatures highlighted in Fig. 2 that are characterized by descending traces are clear signatures of large-scale TIDs, on the order of 100s of kms (e.g., Cervera & Harris, 2014; Pederick et al., 2017). While Spread-F observed at low latitudes is typically associated with EPBs generated by the Generalized Rayleigh-Taylor instability during the post-sunset to local midnight hours (Sultan, 1996; Burke et al., 2004; Kelley et al., 2006; Carter et al., 2014, 2020, and references therein), mid-latitude Spread-F is generally considered to be due to the Perkins instability (e.g., Perkins, 1973; Kelley & Fukao, 1991) or specular reflections from medium-scale TIDs with scales on the order of 10s of kms (e.g., G. Bowman, 1981; G. G. Bowman & Monro, 1988; G. G. Bowman, 1990). Interestingly, the results in Fig. 6 do not appear to show a clear and consistent relationship between the presence of large-scale TIDs or medium-scale TIDs/spread F and increased PPP convergence times.

The GPS stations used in this study are not high-rate receivers that enable a detailed analysis into the full spectrum of ionospheric waves (e.g., Cervera & Thomas, 2006; van de Kamp & Cannon, 2009; Carrano et al., 2012). However, given the apparent motion of the GPS satellites above ground-based receivers and assuming typical ionospheric wave phase speeds, the GPS ROTI parameter can provide insight into the presence of ionospheric irregularities on the order of a few kms (e.g., Pi et al., 1997; Ma & Maruyama, 2006; Nishioka et al., 2008; Zou & Wang, 2009). Generally speaking, there is quite good agreement between the impact on the convergence time and enhanced ROTI, by comparing Figs. 6 and 8 and comparing Figs. 7 and 9. Although, one noted difference was the presence of enhanced ROTI that propagated over southeast Australia and then disappeared. The propagation of this ROTI disturbance agrees well with the propagation of the Lamb wave across the region reported by Aa et al. (2022) (see their Fig. 4). From these observations, one can conclude that the large-scale TIDs caused by the eruption had secondary small-scale irregularity generation all the way down to the scale of kms, making them detectable using the ROTI parameter. Although, an open question that arises is why did these secondary waves not continue to propagate across southern Australia? In other words, what caused the small-scale irregularities over southeast Australia at 9 UT in Fig. 9d to either no longer be generated – or be more heavily damped – by 10 UT in Fig. 9e, when the presence of the Lamb wave in the ROTI data was still clear over northern Australia? The answer either lies in the differences in the effectiveness of the energy cascade from large-scale to small-scale waves, or in the factors that control the damping of small-scale structures between northern and southern Australia. In either case, this is one interesting observation that requires further study and explanation.

In terms of the impact of ionospheric irregularities on the PPP convergence time, these results suggest that increased ROTI – and therefore the presence of small-scale (i.e., km-scale) ionospheric irregularities – tends to prolong PPP convergence times only in the event that the period of increased ROTI lasts for 30 mins or longer. This likely explains why stations in Australia's northern region are clearly impacted compared to the stations in southern and central Australia in Fig. 7. Therefore, an ongoing challenge for the GPS PPP community is to effectively mitigate the adverse impacts of extended periods of small-scale ionospheric irregularity activity.

The next question is by what physical mechanism are these small-scale ionospheric irregularities being generated in order to have such a detrimental impact on GPS PPP? At first glance, the most heavily influenced region in northeastern Australia are too far south for typical EPBs to be an obvious likely candidate. At 400 km above Townsville (i.e., the IPP), the magnetic latitude is 31.5°S, and the magnetic field line from this location maps to the equator at an altitude close to 2100 km; using a combination of the International Geomagnetic Reference Field (Maus et al., 2005; IAGA, 2010) and the Altitude Adjustment Corrected Geomagnetic (AACGM) (Baker & Wing, 1989; Laundal & Richmond, 2017) models. While some observations have been reported of such EPBs in the past (Ma & Maruyama, 2006; Cherniak & Zakharenkova, 2016), disturbances this large are particularly uncommon. Further, EPBs in the Southeast Asian/Australian longitude sector are not commonly observed during the months surrounding the December solstice (e.g., Burke et al., 2004; Nishioka et al., 2008; E. Dao et al., 2011; Carter et al., 2014, 2020). However, Aa et al. (2022) and Rajesh et al. (2022) recently reported observations of EPBs in the vicinity of Australia in the hours following the eruption. The detection of strong spread-F traces by the Townsville ionosonde coincides with local times that are typical of postsunset EPBs; i.e., 21-01 LT (see Fig. 2). Further, plots of VTEC in Fig. 10 in this study agree well with the observations reported by Rajesh et al. (2022) in revealing the presence of a deep depletion over northeastern Australia. Here, we measure that depletion to be 48 TECU on the ridges and 6 TECU in the valley. The propagation of this depletion was determined in this study to be eastwards (Fig. 11), on the order of 30 m/s. If this TEC depletion was a signature of TIDs propagating away from the eruption, then the propagation would have been westwards. Moreover, if it were TIDs from Tonga then the propagation would have been expected to much larger than 30 m/s. Such low eastward propagation speeds are typical of the F-region dynamo in the dusk sector, within which EPBs drift following their non-linear growth to the topside F region (e.g., Kelley, 2009; Chapagain et al., 2013, and references therein). Therefore, the local time of the Spread-F observed over Townsville, the VTEC depletion depth of 42 TECU and the associated eastward propagation speed in results presented here strongly indicate that the structure responsible for hours of increased ROTI, and subsequently increased PPP convergence times, in northeastern Australia is an EPB, in agreement with Rajesh et al. (2022).

It can be seen from the full animation of Fig. 11 (Supplementary Material (S3)) that data points associated with the depletion over northeastern Australia appeared as far south as 18°S, equivalent to 30°S magnetic latitude with an apex altitude of 1900 km over the magnetic equator. The authors are unaware of any other previously reported EPB disturbance that has been observed this far south over the Australian continent before, although similar-sized EPBs (referred to as 'super bubbles' due to their high altitude) have been reported using dense GPS stations across Japan (Ma & Maruyama, 2006). The EPBs that featured in that study would have also appeared over Australia due to magnetic conjugacy, but the relative sparsity of GPS stations across northern Australia did not allow clear EPB observations. However, the density of GPS stations across northern Australia has improved significantly during the solar cycle since Ma and Maruyama (2006)'s study. It is also worth highlighting that elements of Figs. 10 and 11 indicate the presence of TEC depletions farther to the south, but the sparsity of data at these locations makes a clear separation of TID disturbances from EPB-like disturbances difficult for this event. Further, the low density of GPS stations (and therefore, IPPs) across the rest of northern Australia makes a clear determination of whether depletions/EPBs were present difficult in this analysis. However, the impact on PPP convergence times across the rest of northern Australia and southeast Asia shown in Fig. 7 strongly suggests the ongoing presence of EPBs throughout the region during this event; a result in good agreement with the observations of Sun, Wenjie et al. (2022) and Aa et al. (2022) (in particular, the ICON plasma density depletions shown to the north of Australia in their Fig. 6). Some key insights into how TIDs from the eruption caused unseasonal EPB activity in the western Pacific sector can be gained from recent work by Huba et al. (2022). In Huba et al. (2022)'s modeling analysis, waves launched by the eruption caused significant perturbations in the zonal neutral wind in the equatorial plane, which effectively modified the equatorial upward plasma drift and gave rise to a huge EPB that spanned 30° in longitude (between 140-170°E). Huba et al. (2022) referred to this EPB as a 'super EPB' due to its large longitudinal extent. In addition, two very-high-altitude EPBs that reached 4000 km at $\sim$ 155°E and 180° were also generated by their simulation (altitudes well above those that Ma and Maruyama (2006) referred to as 'super bubbles' in their study). While the 30°-wide EPB in Huba et al. (2022)'s simulation was not clearly observed in the present study (possibly due to its limited latitudinal extent), the observation of a longitudinally narrow, high-altitude and low-density structure over northeastern Australia is consistent with the very-high-altitude EPBs in Huba et al. (2022)'s study; noting the rather reasonable differences in observed versus modeled location. This structure over northeastern Australia thus fits the definition of a 'super bubble' according to Ma and Maruyama (2006) and is in good agreement with the results of Rajesh et al. (2022). The impacts on GPS reported in the present study across the rest of northern Australia indicate that further analysis of this event farther towards the west across southern and southeastern Asia is needed.

## 5 Conclusions

The Hunga Tonga Volcano eruption is a unique and complicated event that has provided an unprecedented opportunity to study how the ionosphere couples to the lower atmosphere. In this study, the impact of the eruption – via the ionospheric disturbances that it generated – on GPS PPP was investigated. While static-mode PPP accuracy itself did not appear to be heavily affected, the time taken for convergence to be achieved was found to be significantly impacted. Across northern Australia the impact was particularly clear, with some GPS stations near Townsville reporting increases in convergence time of more than 5 hours. Long convergence times are limiting the widespread use of PPP, so the Hunga Tonga Volcano eruption presents a good opportunity to research the impacts and vulnerabilities of a variable ionosphere on PPP and to learn how to mitigate/account for them.

In this study, it was found that large- and medium-scale TIDs from the eruption were not the cause of convergence time increases, but it was the presence of small-scale ionospheric structures on the order of a few kms, as determined using the ROTI parameter. Further, it was revealed that PPP was robust enough to endure some enhanced ROTI, but not if the duration is longer than $\sim$ 30 mins. This observation effectively differentiated the impact observed on PPP in northern and southern Australia; northern Australia/southeast Asia experienced extended periods of increased ROTI and subsequently increased convergence times, whereas southern Australia only experienced a short burst of increased ROTI with marginal impact on convergence time.

The results of this study indicate that the ionospheric phenomenon responsible for the presence of small-scale irregularities in southern and northern Australia was different. In southern Australia, the small-scale irregularities were the result of secondary generation from the large- and medium-scale TIDs propagating away from the eruption. The enhanced ROTI region propagated to the west in a manner consistent with the Lamb waves previously reported. These small-scale structures were rather promptly damped and did not propagate far beyond southeastern Australia. In northern Australia, the extended periods of enhanced ROTI were found to be due to the presence of at least one 'super bubble' that was observed as far south as $\sim$30°S magnetic latitude, with an estimated apex altitude of $\sim$ 1900 km above the magnetic equator; this is the same 'super EPB' recently reported by Rajesh et al. (2022). The VTEC data revealed that the EPB was $\sim$ 42 TECU deep and $\sim$ 300 km across in longitude. Further, it was shown that the EPB traveled eastwards at $\sim$ 30 m/s, consistent with the F-region dynamo speed and direction. This super bubble is the largest/most southward-reaching EPB observed over the Australian continent; only recently made possible due to GPS station deployments in the region.

The Hunga Tonga Volcano eruption stands as an excellent example of how ionospheric variability can adversely influence satellite-based precise positioning that is increasingly heavily relied upon across many industries and sectors around the world.

## 6 Open Research

The Bureau of Meteorology Space Weather Services' World Data Centre provides ionosonde data via their website; https://www.sws.bom.gov.au/World_Data_Centre. Geoscience Australia provides GNSS data for all of the stations used in this analysis via their Global Navigation Satellite System Data Centre; https://gnss.ga.gov.au/. Geoscience Australia's Ginan platform is also accessible via their github repository; https://geoscienceaustralia.github.io/ginan/. The higher level analysis products, particularly the PPP convergence times that were calculated using Ginan, are available on the Zenodo data repository (doi:10.5281/zenodo.7694409).

**Acknowledgments**

B. A. Carter, S. Choy and T. Dao would like to acknowledge the support of FrontierSI (project PA1002A). M. Le Huy was supported by the Vietnam Academy of Science and Technology under the grant number NVCC 12.02/22-22. R. Pradipta's time was partially supported by grant FA9550-20-1-0313 from the Air Force Office of Scientific Research. The authors would also like to acknowledge the advice and assistance of R. Maj in running Geoscience Australia's Ginan platform.

## References

Aa, E., Zhang, S.-R., Erickson, P. J., Vierinen, J., Coster, A. J., Goncharenko, L. P., ... Rideout, W. (2022). Significant Ionospheric Hole and Equatorial Plasma Bubbles After the 2022 Tonga Volcano Eruption. *Space Weather*, *20*(7), e2022SW003101. doi: https://doi.org/10.1029/2022SW003101

Astafyeva, E., Maletckii, B., Mikesell, T. D., Munaibari, E., Ravanelli, M., Coisson, P., ... Rolland, L. (2022). The 15 January 2022 Hunga Tonga Eruption History as Inferred From Ionospheric Observations. *Geophysical Research Letters*, *49*(10), e2022GL098827. doi: https://doi.org/10.1029/2022GL098827

Baker, K. B., & Wing, S. (1989). A new magnetic coordinate system for conjugate studies at high latitudes. *Journal of Geophysical Research: Space Physics*, *94*(A7), 9139–9143. doi: https://doi.org/10.1029/JA094iA07p09139

Banville, S., Collins, P., Zhang, W., & Langley, R. B. (2014). Global and Regional Ionospheric Corrections for Faster PPP Convergence. *Navigation*, *61*(2), 115-124. doi: https://doi.org/10.1002/navi.57

Bisnath, S., & Gao, Y. (2009). Current state of precise point positioning and future prospects and limitations. In *Observing our changing earth* (pp. 615–623). Springer.

Borries, C., Jakowski, N., & Wilken, V. (2009). Storm induced large scale tids observed in gps derived tec. *Annales Geophysicae*, *27*(4), 1605–1612. doi: https://doi.org/10.5194/angeo-27-1605-2009

Bowman, G. (1981). The nature of ionospheric spread-F irregularities in mid-latitude regions. *Journal of Atmospheric and Terrestrial Physics*, *43*(1), 65-79. doi: https://doi.org/10.1016/0021-9169(81)90010-6

Bowman, G. G. (1990). A review of some recent work on mid-latitude spread-¡i¿f¡/i¿ occurrence as detected by ionosondes. *Journal of geomagnetism and geoelectricity*, *42*(2), 109-138. doi: https://doi.org/10.5636/jgg.42.109

Bowman, G. G., & Monro, P. E. (1988). Mid-latitude range spread and travelling ionospheric disturbances. *Journal of Atmospheric and Terrestrial Physics*, *50*(3), 215-223. doi: https://doi.org/10.1016/0021-9169(88)90070-0

Burke, W. J., Gentile, L. C., Huang, C. Y., Valladres, C. E., & Su, S. Y. (2004). Longitudinal variability of equatorial plasma bubbles observed by DMSP and ROCSAT-1. *J. Geophys. Res.*, *109*. (A12301) doi: https://doi.org/10.1029/2004JA010583

Carrano, C. S., Valladares, C. E., & Groves, K. M. (2012). Latitudinal and local time variation of ionospheric turbulence parameters during the conjugate point equatorial experiment in Brazil. *International Journal of Geophysics*, *2012*.

Carter, B. A., Currie, J. L., Dao, T., Yizengaw, E., Retterer, J., Terkildsen, M., ... Caton, R. (2020). On the Assessment of Daily Equatorial Plasma Bubble Occurrence Modeling and Forecasting. *Space Weather*, *18*(9), e2020SW002555. doi: https://doi.org/10.1029/2020SW002555

Carter, B. A., Ram, S. T., Yizengaw, E., Pradipta, R., Retterer, J., Norman, R., ... others (2018). Unseasonal development of post-sunset F-region irregularities over Southeast Asia on 28 July 2014: 1. Forcing from above? *Progress in Earth and Planetary Science*, *5*(1), 1–12.

Carter, B. A., Yizengaw, E., Retterer, J. M., Francis, M., Terkildsen, M., Marshall, R., ... Zhang, K. (2014). An analysis of the quiet-time day-to-day variability in the formation of post-sunset equatorial plasma bubbles in the Southeast Asian region. *J. Geophys. Res.*, *119*, 3206–3223. doi: https://doi.org/10.1002/2013JA019570

Carvajal, M., Sepúlveda, I., Gubler, A., & Garreaud, R. (2022). Worldwide signature of the 2022 tonga volcanic tsunami. *Geophysical Research Letters*, *49*(6), e2022GL098153. doi: https://doi.org/10.1029/2022GL098153

Cervera, M. A., & Harris, T. J. (2014). Modeling ionospheric disturbance features in quasi-vertically incident ionograms using 3-d magnetoionic ray tracing and atmospheric gravity waves. *Journal of Geophysical Research: Space Physics*, *119*(1), 431-440. doi: https://doi.org/10.1002/2013JA019247

Cervera, M. A., & Thomas, R. M. (2006). Latitudinal and temporal variation of equatorial ionospheric irregularities determined from GPS scintillation observations. *Annales Geophysicae*, *24*(12), 3329–3341. doi: https://doi.org/10.5194/angeo-24-3329-2006

Chapagain, N. P., Fisher, D. J., Meriwether, J. W., Chau, J. L., & Makela, J. J. (2013). Comparison of zonal neutral winds with equatorial plasma bubble and plasma drift velocities. *Journal of Geophysical Research: Space Physics*, *118*(4), 1802-1812. doi: https://doi.org/10.1002/jgra.50238

Cherniak, I., & Zakharenkova, I. (2016). First observations of super plasma bubbles in Europe. *Geophysical Research Letters*, *43*(21), 11,137-11,145. doi: https://doi.org/10.1002/2016GL071421

Choy, S., Bisnath, S., & Rizos, C. (2017). Uncovering common misconceptions in GNSS Precise Point Positioning and its future prospect. *GPS solutions*, *21*(1), 13–22.

Collins, P., & Bisnath, S. (2011). Issues in Ambiguity Resolution for Precise Point Positioning. In *Proceedings of the 24th international technical meeting of the satellite division of the institute of navigation (ion gnss 2011)* (pp. 679–687).

Collins, P., Lahaye, F., & Bisnath, S. (2012). External ionospheric constraints for improved PPP-AR initialisation and a generalised local augmentation concept. In *Proceedings of the 25th international technical meeting of the satellite division of the institute of navigation (ion gnss 2012)* (pp. 3055–3065).

Currie, J., Carter, B., Retterer, J., Dao, T., Pradipta, R., Caton, R., ... others (2021). On the generation of an unseasonal EPB over South East Asia. *Journal of Geophysical Research: Space Physics*, *126*(2), e2020JA028724. doi: https://doi.org/10.1029/2020JA028724

Dao, E., Kelley, M. C., Roddy, P., Retterer, J., Ballenthin, J. O., de La Beaujardiere, O., & Su, Y.-J. (2011). Longitudinal and seasonal dependence of nighttime equatorial plasma density irregularities during solar minimum detected on the C/NOFS satellite. *Geophys. Res. Lett.*, *38*. doi: https://doi.org/10.1029/2011GL047046

Dao, T., Le Huy, M., Carter, B., Le, Q., Trinh, T. T., Phan, B. N., & Otsuka, Y. (2020). New observations of the total electron content and ionospheric scintillations over Ho Chi Minh City. *Science of the Earth*, *42*(4), 320–333. doi: 10.15625/0866-7187/42/4/15281

Díaz, J., & Rigby, S. (2022). Energetic output of the 2022 Hunga Tonga–Hunga Ha 'apai volcanic eruption from pressure measurements. *Shock Waves*, *32*(6), 553–561.

Duong, V. T. (2020). *Precise Point Positioning with ambiguity resolution using multi-frequency multi-constellation GNSS measurements* (PhD Thesis). RMIT University.

Geng, J., & Bock, Y. (2013). Triple-frequency GPS precise point positioning with rapid ambiguity resolution. *Journal of geodesy*, *87*, 449–460.

Ghent, J. N., & Crowell, B. W. (2022). Spectral Characteristics of Ionospheric Disturbances Over the Southwestern Pacific From the 15 January 2022 Tonga Eruption and Tsunami. *Geophysical Research Letters*, *49*(20), e2022GL100145. doi: https://doi.org/10.1029/2022GL100145

Harding, B. J., Wu, Y.-J. J., Alken, P., Yamazaki, Y., Triplett, C. C., Immel, T. J., ... Xiong, C. (2022). Impacts of the January 2022 Tonga Volcanic Eruption on the Ionospheric Dynamo: ICON-MIGHTI and Swarm Observations of

Extreme Neutral Winds and Currents. *Geophysical Research Letters*, *49*(9), e2022GL098577. doi: https://doi.org/10.1029/2022GL098577

Hofmann-Wellenhof, B., Lichtenegger, H., & Wasle, E. (2007). *GNSS–Global Navigation Satellite Systems: GPS, GLONASS, Galileo, and more.* Springer Science & Business Media.

Hong, J., Kil, H., Lee, W. K., Kwak, Y.-S., Choi, B.-K., & Paxton, L. J. (2022). Detection of Different Properties of Ionospheric Perturbations in the Vicinity of the Korean Peninsula After the Hunga-Tonga Volcanic Eruption on 15 January 2022. *Geophysical Research Letters*, *49*(14), e2022GL099163. doi: https://doi.org/10.1029/2022GL099163

Huba, J., Becker, E., & Vadas, S. (2022). Simulation Study of the 15 January 2022 Tonga Event: Development of Super Equatorial Plasma Bubbles. *Geophysical Research Letters*, e2022GL101185. doi: https://doi.org/10.1029/2022GL101185

IAGA. (2010). *International Geomagnetic Reference Field - 11th Generation.* (NOAA National Centers for Environmental Information) doi: https://doi.org/10.7289/V58050JN

Johnston, G., Riddell, A., & Hausler, G. (2017). The international GNSS service. In *Springer handbook of global navigation satellite systems* (pp. 967–982). Springer.

Kelley, M. C. (2009). *The Earth's Ionosphere: Plasma Physics and Electrodynamics* (2nd ed.). Elsevier, London.

Kelley, M. C., & Fukao, S. (1991). Turbulent upwelling of the mid-latitude ionosphere: 2. Theoretical framework. *Journal of Geophysical Research: Space Physics*, *96*(A3), 3747-3753. doi: https://doi.org/10.1029/90JA02252

Kelley, M. C., Makela, J. J., & de La Beaujardiére, O. (2006). Convective ionospheric storms: A major space weather problem. *Space Weather*, *4*. doi: 10.1029/2005SW000144

Klobuchar, J. A. (1986). Design and characteristics of the GPS ionospheric time delay algorithm for single frequency users. In *Plans'86-position location and navigation symposium* (pp. 280–286).

Kotake, N., Otsuka, Y., Tsugawa, T., Ogawa, T., & Saito, A. (2006). Climatological study of gps total electron content variations caused by medium-scale traveling ionospheric disturbances. *Journal of Geophysical Research: Space Physics*, *111*(A4). doi: https://doi.org/10.1029/2005JA011418

Kouba, J., Lahaye, F., & Tétreault, P. (2017). Precise Point Positioning. In P. J. Teunissen & O. Montenbruck (Eds.), *Springer handbook of global navigation satellite systems* (pp. 723–751). Cham: Springer International Publishing. doi: https://doi.org/10.1007/978-3-319-42928-1_25

Laundal, K. M., & Richmond, A. D. (2017). Magnetic coordinate systems. *Space Science Reviews*, *206*(1-4), 27–59.

Lay, E. H., Parker, P. A., Light, M., Carrano, C. S., Debchoudhury, S., & Haaser, R. A. (2018). Midlatitude Ionospheric Irregularity Spectral Density as Determined by Ground-Based GPS Receiver Networks. *Journal of Geophysical Research: Space Physics*, *123*(6), 5055-5067. doi: https://doi.org/10.1029/2018JA025364

Le, G., Liu, G., Yizengaw, E., & Englert, C. R. (2022). Intense Equatorial Electrojet and Counter Electrojet Caused by the 15 January 2022 Tonga Volcanic Eruption: Space- and Ground-Based Observations. *Geophysical Research Letters*, *49*(11), e2022GL099002. doi: https://doi.org/10.1029/2022GL099002

Le Huy, M., Tran Thi, L., Fleury, R., Amory-Mazaudier, C., Le Truong, T., Nguyen Chien, T., & Nguyen Ha, T. (2016). TEC variations and ionospheric disturbances during the magnetic storm in March 2015 observed from continuous GPS data in the Southeast Asia region. *Vietnam Journal of Earth Sciences*, *38*(3), 287–305. doi: https://doi.org/10.15625/0866-7187/38/3/8714

Leick, A., Rapoport, L., & Tatarnikov, D. (2015). *GPS satellite surveying.* John Wiley & Sons.

Li, X., Zhang, X., Ren, X., Fritsche, M., Wickert, J., & Schuh, H. (2015). Precise positioning with current multi-constellation global navigation satellite systems: GPS, GLONASS, Galileo and BeiDou. *Scientific reports*, *5*(1), 1–14.

Luo, X., Du, J., Lou, Y., Gu, S., Yue, X., Liu, J., & Chen, B. (2022). A Method to Mitigate the Effects of Strong Geomagnetic Storm on GNSS Precise Point Positioning. *Space Weather*, *20*(1), e2021SW002908. doi: https://doi.org/10.1029/2021SW002908

Luo, X., Gu, S., Lou, Y., Xiong, C., Chen, B., & Jin, X. (2018). Assessing the Performance of GPS Precise Point Positioning Under Different Geomagnetic Storm Conditions during Solar Cycle 24. *Sensors*, *18*(6). doi: https://doi.org/10.3390/s18061784

Ma, G., & Maruyama, T. (2006). A super bubble detected by dense GPS network at east Asian longitudes. *Geophysical Research Letters*, *33*(21). doi: https://doi.org/10.1029/2006GL027512

Maletckii, B., & Astafyeva, E. (2022). Near-Real-Time Analysis of the Ionospheric Response to the 15 January 2022 Hunga Tonga-Hunga Ha'apai Volcanic Eruption. *Journal of Geophysical Research: Space Physics*, *127*(10), e2022JA030735. doi: https://doi.org/10.1029/2022JA030735

Mannucci, A., Wilson, B., Yuan, D., Ho, C., Lindqwister, U., & Runge, T. (1998). A global mapping technique for GPS-derived ionospheric total electron content measurements. *Radio science*, *33*(3), 565–582.

Matoza, R. S., Fee, D., Assink, J. D., Iezzi, A. M., Green, D. N., Kim, K., ... Wilson, D. C. (2022). Atmospheric waves and global seismoacoustic observations of the January 2022 Hunga eruption, Tonga. *Science*, *377*(6601), 95-100. doi: https://doi.org/10.1126/science.abo7063

Maus, S., Macmillan, S., Chernova, T., Choi, S., Dater, D., Golovkov, V., ... Zvereva, T. (2005). The 10th generation international geomagnetic reference field. *Phys. Earth Planet. Inter.*, *151*, 320-322.

Nishioka, M., Saito, A., & Tsugawa, T. (2008). Occurrence characteristics of plasma bubble derived from global ground-based GPS receiver networks. *J. Geophys. Res.*, *113*. (A05301) doi: 10.1029/2007JA012605

Odijk, D. (2002). Fast precise GPS positioning in the presence of ionospheric delays. *Publications on Geodesy, 52*.

Otsuka, Y., Ogawa, T., Saito, A., Tsugawa, T., Fukao, S., & Miyazaki, S. (2002). A new technique for mapping of total electron content using GPS network in Japan. *Earth, planets and space*, *54*(1), 63–70.

Pederick, L. H., Cervera, M. A., & Harris, T. J. (2017). Interpreting observations of large-scale traveling ionospheric disturbances by ionospheric sounders. *Journal of Geophysical Research: Space Physics*, *122*(12), 12,556-12,569. doi: https://doi.org/10.1002/2017JA024337

Perkins, F. (1973). Spread f and ionospheric currents. *Journal of Geophysical Research*, *78*(1), 218-226. doi: https://doi.org/10.1029/JA078i001p00218

Pi, X., Mannucci, A., Lindqwister, U., & Ho, C. (1997). Monitoring of global ionospheric irregularities using the worldwide GPS network. *Geophysical Research Letters*, *24*(18), 2283–2286.

Poniatowski, M., & Nykiel, G. (2020). Degradation of Kinematic PPP of GNSS Stations in Central Europe Caused by Medium-Scale Traveling Ionospheric Disturbances During the St. Patrick's Day 2015 Geomagnetic Storm. *Remote Sensing*, *12*(21). doi: https://doi.org/10.3390/rs12213582

Pradipta, R., Carter, B. A., Currie, J., Choy, S., Wilkinson, P., Maher, P., & Marshall, R. (2023). n the Propagation of Traveling Ionospheric Disturbances from the Hunga Tonga-Hunga Ha'apai Volcano Eruption and their Possible Connection with Tsunami Waves. *Geophysical Research Letters*, 2022GL101925, accepted 3-Mar-2023.

Pradipta, R., Valladares, C. E., Carter, B. A., & Doherty, P. H. (2016). Interhemispheric propagation and interactions of auroral traveling ionospheric disturbances near the equator. *Journal of Geophysical Research: Space Physics*, *121*(3), 2462-2474. doi: https://doi.org/10.1002/2015JA022043

Pradipta, R., Valladares, C. E., & Doherty, P. H. (2015). Ionosonde observations of ionospheric disturbances due to the 15 February 2013 Chelyabinsk meteor explosion. *Journal of Geophysical Research: Space Physics*, *120*(11), 9988-9997. doi: https://doi.org/10.1002/2015JA021767

Pyle, D. M. (2015). Sizes of volcanic eruptions. In *The encyclopedia of volcanoes* (pp. 257–264). Elsevier.

Pérez-Ruiz, M., de Santos, P. G., Ribeiro, A., Fernandez-Quintanilla, C., Peruzzi, A., Vieri, M., … Agüera, J. (2015). Highlights and preliminary results for autonomous crop protection. *Computers and Electronics in Agriculture*, *110*, 150-161. doi: https://doi.org/10.1016/j.compag.2014.11.010

Rajesh, P. K., Lin, C. C. H., Lin, J. T., Lin, C. Y., Liu, J. Y., Matsuo, T., … Tsai, H. F. (2022). Extreme Poleward Expanding Super Plasma Bubbles Over Asia-Pacific Region Triggered by Tonga Volcano Eruption During the Recovery-Phase of Geomagnetic Storm. *Geophysical Research Letters*, *49*(15), e2022GL099798. doi: https://doi.org/10.1029/2022GL099798

Rao, A. S., Radanovic, M., Liu, Y., Hu, S., Fang, Y., Khoshelham, K., … Ngo, T. (2022). Real-time monitoring of construction sites: Sensors, methods, and applications. *Automation in Construction*, *136*, 104099. doi: https://doi.org/10.1016/j.autcon.2021.104099

Sultan, P. J. (1996). Linear theory and modeling of the Rayleigh-Taylor instability leading to the occurrence of equatorial spread F. *J. Geophys. Res.*, *101*, 26875-26891.

Sun, Wenjie, Kaippallimyalil Kuriakose, Ajith, Li, Guozhu, Li, Yu, Zhao, Xiukuan, Hu, Lianhuan, … Liu, Libo (2022). Unseasonal super ionospheric plasma bubble and scintillations seeded by the 2022 Tonga Volcano Eruption related perturbations. *J. Space Weather Space Clim.*, *12*, 25. doi: https://doi.org/10.1051/swsc/2022024

Teunissen, P. J., & Montenbruck, O. (2017). *Springer handbook of global navigation satellite systems* (Vol. 10). Springer.

Themens, D. R., Watson, C., Žagar, N., Vasylkevych, S., Elvidge, S., McCaffrey, A., … Jayachandran, P. T. (2022). Global propagation of ionospheric disturbances associated with the 2022 tonga volcanic eruption. *Geophysical Research Letters*, *49*(7), e2022GL098158. doi: https://doi.org/10.1029/2022GL098158

Tsugawa, T., Saito, A., Otsuka, Y., Nishioka, M., Maruyama, T., Kato, H., … Murata, K. (2011). Ionospheric disturbances detected by GPS total electron content observation after the 2011 off the Pacific coast of Tohoku Earthquake. *Earth, planets and space*, *63*(7), 875–879.

Van Bree, R. J., Tiberius, C. C., & Hauschild, A. (2009). Real time satellite clocks in single frequency precise point positioning. In *Proceedings of the 22nd international technical meeting of the satellite division of the institute of navigation (ion gnss 2009)* (pp. 2400–2414).

van de Kamp, M. M. J. L., & Cannon, P. S. (2009). Spectra of equatorial total electron content derived from GPS signals. *Annales Geophysicae*, *27*(5), 2205–2214. doi: https://doi.org/10.5194/angeo-27-2205-2009

Vergoz, J., Hupe, P., Listowski, C., Le Pichon, A., Garcés, M., Marchetti, E., … Mialle, P. (2022). IMS observations of infrasound and acoustic-gravity waves produced by the January 2022 volcanic eruption of Hunga, Tonga: A global analysis. *Earth and Planetary Science Letters*, *591*, 117639. doi: https://doi.org/10.1016/j.epsl.2022.117639

Woodgate, P., Coppa, I., Choy, S., Phinn, S., Arnold, L., & Duckham, M. (2017).

The Australian approach to geospatial capabilities; positioning, earth observation, infrastructure and analytics: issues, trends and perspectives. *Geo-spatial information science*, *20*(2), 109–125.

Wright, C. J., Hindley, N. P., Alexander, M. J., Barlow, M., Hoffmann, L., Mitchell, C. N., ... Yue, J. (2022). Surface-to-space atmospheric waves from Hunga Tonga–Hunga Ha'apai eruption. *Nature*, *609*(7928), 741–746. doi: https://doi.org/10.1038/s41586-022-05012-5

Yang, H., Monte-Moreno, E., & Hernández-Pajares, M. (2017). Multi-TID detection and characterization in a dense Global Navigation Satellite System receiver network. *Journal of Geophysical Research: Space Physics*, *122*(9), 9554-9575. doi: https://doi.org/10.1002/2017JA023988

Yang, Z., Morton, Y. T. J., Zakharenkova, I., Cherniak, I., Song, S., & Li, W. (2020). Global View of Ionospheric Disturbance Impacts on Kinematic GPS Positioning Solutions During the 2015 St. Patrick's Day Storm. *Journal of Geophysical Research: Space Physics*, *125*(7), e2019JA027681. doi: https://doi.org/10.1029/2019JA027681

Yizengaw, E., Moldwin, M., Galvan, D., Iijima, B., Komjathy, A., & Mannucci, A. (2008). Global plasmaspheric TEC and its relative contribution to GPS TEC. *Journal of Atmospheric and Solar-Terrestrial Physics*, *70*(11-12), 1541–1548.

Zakharenkova, I., & Cherniak, I. (2021). Effects of storm-induced equatorial plasma bubbles on GPS-based kinematic positioning at equatorial and middle latitudes during the September 7–8, 2017, geomagnetic storm. *GPS Solutions*, *25*(4), 1–14. doi: https://doi.org/10.1007/s10291-021-01166-3

Zha, J., Zhang, B., Liu, T., & Hou, P. (2021). Ionosphere-weighted undifferenced and uncombined PPP-RTK: theoretical models and experimental results. *GPS Solutions*, *25*(4), 1–12.

Zhang, H., Gao, Z., Ge, M., Niu, X., Huang, L., Tu, R., & Li, X. (2013). On the Convergence of Ionospheric Constrained Precise Point Positioning (IC-PPP) Based on Undifferential Uncombined Raw GNSS Observations. *Sensors*, *13*(11), 15708–15725. doi: https://doi.org/10.3390/s131115708

Zhang, S.-R., Vierinen, J., Aa, E., Goncharenko, L. P., Erickson, P. J., Rideout, W., ... Spicher, A. (2022). 2022 Tonga Volcanic Eruption Induced Global Propagation of Ionospheric Disturbances via Lamb Waves. *Frontiers in Astronomy and Space Sciences*, *9*. doi: https://doi.org/10.3389/fspas.2022.871275

Zou, Y., & Wang, D. (2009). A study of GPS ionospheric scintillations observed at Guilin. *Journal of Atmospheric and Solar-Terrestrial Physics*, *71*(17-18), 1948–1958.

Zumberge, J. F., Heflin, M. B., Jefferson, D. C., Watkins, M. M., & Webb, F. H. (1997). Precise point positioning for the efficient and robust analysis of GPS data from large networks. *Journal of Geophysical Research: Solid Earth*, *102*(B3), 5005-5017. doi: https://doi.org/10.1029/96JB03860

# The ionospheric effects of the 2022 Hunga Tonga Volcano eruption and the associated impacts on GPS Precise Point Positioning across the Australian region

**B. A. Carter[1], R. Pradipta[2], T. Dao[1], J. L. Currie[1], S. Choy[1], P. Wilkinson[3], P. Maher[4,5], R. Marshall[4], K. Harima[6], M. LeHuy[7], T. Nguyen Chien[7], T. Nguyen Ha[7], T. J. Harris[8]**

[1]School of Science, RMIT University, Melbourne, Australia
[2]Institute for Scientific Research, Boston College, Boston, USA
[3]Ionospheric Prediction Service (retired), Sydney, Australia
[4]Space Weather Services, Bureau of Meteorology, Sydney and Adelaide, Australia
[5]Now at: Riverbed Technology, Australia
[6]FrontierSI, Melbourne, Australia
[7]Institute of Geophysics, Vietnam Academy of Science and Technology (VAST), Hanoi, Vietnam
[8]School of Physical Sciences, The University of Adelaide, Adelaide, Australia

**Key Points:**

- PPP convergence times across northern Australia were significantly impacted in the hours after the eruption
- Extended periods of enhanced ROTI were the cause of convergence time increases
- A super equatorial plasma bubble, the largest observed over Australia, was responsible for PPP convergence time increases after the eruption

Corresponding author: Brett Carter, `brett.carter@rmit.edu.au`

## Abstract

The Hunga Tonga Volcano eruption launched a myriad of atmospheric waves that have been observed to travel around the world several times. These waves generated Traveling Ionospheric Disturbances (TIDs) in the ionosphere, which are known to adversely impact radio applications such as Global Navigation Satellite Systems (GNSS). One such GNSS application is Precise Point Positioning (PPP), which can achieve cm-level accuracy using a single receiver, following a typical convergence time of 30 mins to 1 hour. A network of ionosondes located throughout the Australian region were used in combination with GNSS receivers to explore the impacts of the Hunga-Tonga Volcano eruption on the ionosphere and what subsequent impacts they had on PPP. It is shown that PPP accuracy was not significantly impacted by the arrival of the TIDs and Spread-F, provided that PPP convergence had already been achieved. However, when the PPP algorithm was initiated from a cold start either shortly before or after the TID arrivals, the convergence times were significantly longer. GNSS stations in northeastern Australia experienced increases in convergence time of more than 5 hours. Further analysis reveals increased convergence times to be caused by a super equatorial plasma bubble (EPB), the largest observed over Australia to date. The EPB structure was found to be ∼42 TECU deep and ∼300 km across, traveling eastwards at 30 m/s. The Hunga Tonga Volcano eruption serves as an excellent example of how ionospheric variability can impact real-world applications and the challenges associated with modeling the ionosphere to support GNSS.


## Plain Language Summary

Global Navigation Satellite System (GNSS) applications permeate modern society, with many industry sectors heavily relying on precision satellite positioning, navigation and timing. Precise Point Positioning (PPP) is an advanced positioning technique that can achieve cm-level accuracy without the need for nearby reference stations. However, the time that it takes for the PPP solution to 'converge' is typically in the range of 10s of mins to hours, limiting the widespread uptake of PPP. There are numerous previous reports of waves and disturbances in the ionosphere, which are known to adversely impact GNSS applications. In this study, the impact of the disturbances in the ionosphere caused by the 2022 Hunga Tonga-Hunga Ha'pai Volcano eruption on PPP across the Australian region is investigated. It is found that convergence times increased by more than 5 hours across northern Australia due to small-scale ionospheric turbulence. The source of the turbulence was also found in this analysis to be due to a 'super Equatorial Plasma Bubble' that persisted above northern Australia for several hours. This event serves as an excellent example of how ionospheric disturbances can impact relied upon GNSS applications.

## 1 Introduction

At 04:14:45 UT on January 15, 2022, the Hunga Tonga-Hunga Ha'apai Volcano erupted in what was one of the largest explosions on Earth in modern history (Matoza et al., 2022; Wright et al., 2022). It has been estimated that the eruption released somewhere between $3.7 \times 10^{16}$ to $8.37 \times 10^{17}$ Joules (Wright et al., 2022; Astafyeva et al., 2022; Díaz & Rigby, 2022; Vergoz et al., 2022), making it comparable to the Krakatoa eruption in 1883 (Pyle, 2015). The explosion caused a tsunami that reached all sides of the Pacific Ocean with an observed maximum wave-height of 3.4m on the Chilean shoreline (Carvajal et al., 2022). The eruption was even audible as far away as Alaska, which is some 10,000 km away from Tonga (Matoza et al., 2022). Not surprisingly, the eruption caused a myriad of waves in the atmosphere and ionosphere (Themens et al., 2022; Wright et al., 2022; Aa et al., 2022; Astafyeva et al., 2022; Ghent & Crowell, 2022; Maletckii & Astafyeva, 2022; Hong et al., 2022) that were observed to encircle the Earth multiple times (S.-R. Zhang et al., 2022; Matoza et al., 2022; Pradipta et al., 2023).

Waves in the ionosphere can be remotely detected using Global Navigation Satellite System (GNSS) signals in terms of the delay that the ionospheric plasma imparts upon the signals. The phase delay that is measured is related to the total electron content (TEC) between the GNSS satellite and the receiver, with the majority of the TEC contribution coming from the ionosphere (Yizengaw et al., 2008). An expansive network of ground-based GNSS receivers therefore make it possible to geographically map ionospheric TEC around the world (Mannucci et al., 1998) and track the propagation of any ionospheric waves (e.g., Otsuka et al., 2002; Kotake et al., 2006; Borries et al., 2009; Tsugawa et al., 2011; Pradipta et al., 2016; H. Yang et al., 2017; Lay et al., 2018). To date, a range of ionospheric effects associated with the Hunga Tonga Volcano event have been published, and many of these studies have utilized the International GNSS Service network of receivers (Johnston et al., 2017).

Themens et al. (2022) and S.-R. Zhang et al. (2022) reported both large-scale and medium-scale traveling ionospheric disturbances (TIDs) propagating away from the volcano location. S.-R. Zhang et al. (2022) showed evidence of these TIDs continuing to propagate around the world for at least 4 days. Harding et al. (2022) and Le et al. (2022) observed changes to the equatorial electrojet that were caused by variations in the ionospheric dynamo as a result of the eruption. Aa et al. (2022) reported a localized ionospheric plasma depletion in the vicinity of the volcano and increased Equatorial Plasma Bubble (EPB) activity in the Asia-Oceania low-latitude region, which has been further supported by recent modeling efforts (Huba et al., 2022). Evidence of 'super EPBs' has been reported spanning across Chinese (Sun, Wenjie et al., 2022) and Japanese/Australian (Rajesh et al., 2022) longitude sectors following the eruption. Aa et al. (2022) also reported propagating ionospheric irregularities that exhibited a phase speed that matched the prevailing Lamb mode at $\sim$ 315 m/s.

GNSS Precise Point Positioning (PPP) is an advanced positioning technique that uses dual frequency observations made by a single receiver to achieve cm-level positioning accuracy (Zumberge et al., 1997; Leick et al., 2015; Choy et al., 2017; Teunissen & Montenbruck, 2017). Over the previous few decades, the dominant method for achieving cm-level accuracy has been relative positioning, in which a nearby accurately located reference station is used to determine the precise position of a 'rover' receiver (e.g., Odijk, 2002; Hofmann-Wellenhof et al., 2007; Leick et al., 2015; Teunissen & Montenbruck, 2017). Utilizing a nearby reference station makes it possible to eliminate spatially correlated GNSS observations errors, such as the tropospheric and ionospheric delays imposed on the GNSS signals. Unsurprisingly, this precise positioning capability has now found its way into many applications across several major industries, including mining, agriculture and construction (e.g., Pérez-Ruiz et al., 2015; Choy et al., 2017; Woodgate et al., 2017; Rao et al., 2022). Over recent years, PPP is fast becoming the new global standard for cm-level positioning applications due to its ability to model and account for GNSS observations errors without the need for a nearby reference station. However, the most significant drawback that is limiting the widespread uptake of PPP is the rather long convergence times, which are typically on the order of 10s of mins to hours (Bisnath & Gao, 2009; Van Bree et al., 2009; Choy et al., 2017). As a result, researchers have been investigating methods to significantly reduce PPP convergence times (e.g., Collins & Bisnath, 2011; Collins et al., 2012; Geng & Bock, 2013; H. Zhang et al., 2013; Banville et al., 2014; Li et al., 2015; Duong, 2020). Given the significant influence of the ionosphere on GNSS signals, space weather poses a potential vulnerability to the PPP technique and its anticipated widespread up-take. As such, researchers have also been investigating the impact of solar and geomagnetic activity on PPP (e.g., Luo et al., 2018; Poniatowski & Nykiel, 2020; Z. Yang et al., 2020; Zha et al., 2021; Luo et al., 2022).

The Hunga Tonga Volcano eruption provides a unique opportunity to uncover new fundamental knowledge of the physics of atmosphere-ionosphere coupling. In addition, given the adverse influence of ionospheric variability on GNSS, this event can also pro-


Figure 1: The locations of the ionosondes used in this analysis. Tonga is indicated by the red cross.

vide insights into the impact of such ionospheric disturbances across broader society, particularly in industries that rely heavily on precise GNSS positioning. In this study, the impact of the Tonga volcano eruption on Global Positioning System (GPS) PPP across the Australian region is explored. Supporting this analysis are the data collected by ionosondes throughout the region that show both TID and Spread-F activity in the wake of the volcano eruption. The PPP accuracy throughout the day of the eruption is explored, followed by an analysis of the PPP convergence times from stations located throughout the region. Finally, ionospheric observations using GPS receivers across the region are used to investigate the physical mechanisms causing the disruptions identified in this study.

## 2 Data

In this analysis, the Australian Bureau of Meteorology Space Weather Services' ionosonde data are used. Figure 1 shows the locations of the ionosonde stations (black triangles) and Tonga volcano (red cross). The stations are Niue (NUE5F; 19.07°S, 190.07°E), Norfolk Island (NLK5D; 29.03°S, 167.97°E), Canberra (CBR5F; 35.32°S, 149.00°E), Townsville (TVL5F; 19.63°S, 146.8°E), Darwin (DWN5D; 12.45°S, 130.95°E), Perth (PER5D; 31.94°S, 115.95°E), Learmonth (LEA5D; 22.25°S, 114.08°E) and Cocos Keeling Islands (CCK5F; 12.20°S, 96.80°E). Each ionosonde generates ionograms by sweeping through radio frequencies between 2-22 MHz, transmitting and receiving ionospheric echoes that indicate the electron density for a given virtual height determined by time-of-flight. In this analysis, the ionosonde data were used to indicate the presence of TIDs and spread-F traces.

The ionosonde data complement the primary dataset used in this study, namely the GPS receiver data. GPS Continuously Operating Reference Station (CORS) data from stations located across Australia, spanning into the Southeast Asian region and across the South Pacific, were used in this analysis. While previous works have employed such GPS CORS data to analyze ionospheric TEC fluctuations caused by the eruption, this study focuses on the impact of this eruption on the GPS application of PPP.

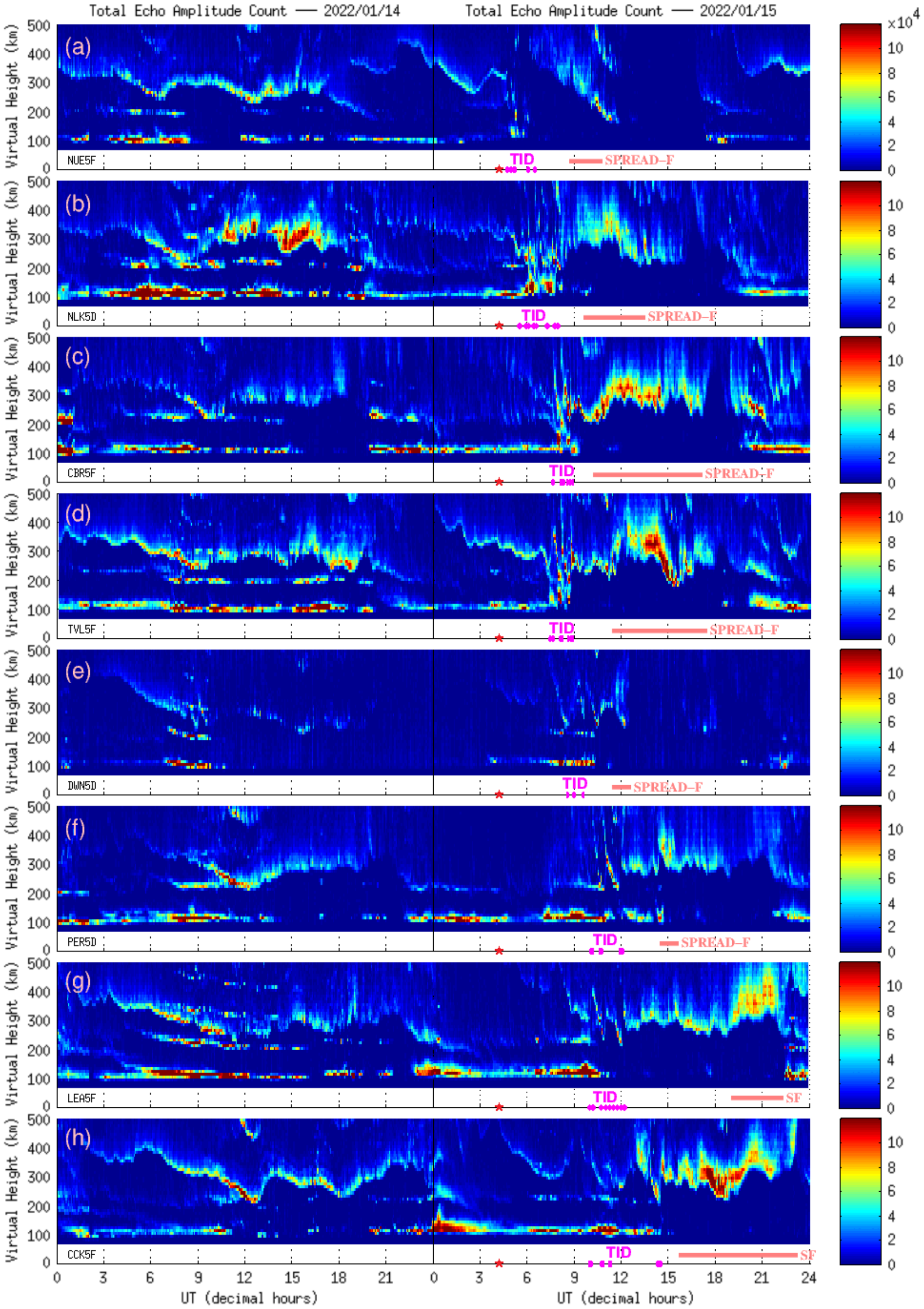


Figure 2: Range-time-intensity-style plots of ionospheric echoes received from ionosondes across the Australian region during January 14-15, 2022. Each panel corresponds to each station; (a) Niue (NUE5F), (b) Norfolk Island (NLK5D), (c) Canberra (CBR5F), (d) Townsville (TVL5F), (e) Darwin (DWN5D), (f) Perth (PER5D), (g) Learmonth (LEA5D) and (h) Cocos Keeling Islands (CCK5F). The color of each bin indicates the number of echoes received in that virtual height bin across all scanning frequencies, as indicated in the color bar on the right. The red stars indicate the time of the eruption; 04:14:45 UT. The pink dots (salmon bars) indicate the presences of TID (Spread-F) signatures.

The Geoscience Australia's Ginan system was used for performing the PPP calculations[1]. PPP is a high accuracy positioning method used to correct errors in GNSS positioning based on the robust modelling and estimations of systematic errors in the GNSS signals. The specific Ginan setup used in this analysis closely follows the Ginan PPP example "Ex11", in which the PPP is performed in 'static mode' using the ionosphere-free combination[2].

The carrier-phase measurements between the GPS satellites and receivers were used to calculate the TEC along the signal path (i.e., the slant TEC, sTEC) following similar methodology to Le Huy et al. (2016) and T. Dao et al. (2020). The possible jumps in the sTEC values estimated from the carrier-phase measurements due to cycle slips were eliminated by comparing them against the sTEC estimated from the pseudo-range measurements that were smoothed by a fourth-degree polynomial approximation. A difference between the carrier-phase sTEC and the pseudo-range sTEC of more than 5 TECU was taken to indicate an instrumental data jump/spike in the carrier-phase sTEC; in such instances, the smoothed pseudo-range sTEC was used. The sTEC was then compared with the Centre of Orbit Determination in Europe Global model to determine the total delay of device (including biases), using elevation angles above 30° to remove multipath effects. Finally, the resulting sTEC was converted to the vertical total electron content (VTEC) observed at the pierce point of the ionosphere by using a single-layer model (Klobuchar, 1986) and an assumed altitude of 400 km.The presence of scintillation-causing small-scale ionospheric irregularities can be detected using the rate of TEC index (ROTI), which is defined as the 5-min standard deviation in the rate of change in the sTEC for each satellite-to-ground link (Pi et al., 1997).

## 3 Results

This analysis begins with an overview of the ionospheric conditions before and after the arrival of the disturbances caused by the volcano eruption using the ionosonde network in Fig. 1. First, it is worth mentioning that a minor geomagnetic storm occurred in the late hours of January 14, with Dst reaching -91 nT due to a small, short-lived recurrent solar wind stream that had a minimal effect on the equatorial electric field (Le et al., 2022). A useful way to analyze temporal changes in ionograms is by representing the data in a format similar to a 'range-time-intensity' plot (Pradipta et al., 2015; Carter et al., 2018; Currie et al., 2021). Instead of using total power, Pradipta et al. (2015) integrated over the dBm amplitudes across all sounding frequencies, effectively creating a sum of digitized echoes. This methodology was adopted for the present study. Figure 2 shows these range-time-intensity-style plots for the ionosondes during January 14-15, 2022; the panels are ordered by the station great circle distance to Tonga, closest to farthest. The colors indicate the number of echoes received across all frequencies in each virtual height bin (10 kms). The presence of TIDs and spread-F traces are indicated at the bottom of each plot by the pink dots and salmon bars, respectively; these have been determined by visual inspection of the ionograms.

Figure 2 shows a range of ionospheric conditions across January 14 and 15; e.g., sporadic E features at virtual heights of 100 km are present for all stations at various times and F region traces that display typical altitude changes with time. TID signatures are also clear in the data on January 15 for all stations, beginning at approx. 4:30 UT at Niue (top panel) and at approx. 10 UT at Cocos Keeling Islands, with the other stations showing the TID signatures at times in between. All stations, with the exception of Darwin which was suffering some intermittent hardware issues during this period, show the presence of spread-F traces in the hours following the TIDs, and in all cases,

[1] https://geoscienceaustralia.github.io/ginan/
[2] https://geoscienceaustralia.github.io/ginan/codeDocs/Pea_8Configuration_8Examples.html

the spread-F traces are persistent for a number of hours. In particular, the TID activity at Norfolk Island begins shortly before 6 UT, with Spread-F present from 09:15 UT until 13:30 UT. Thus, the occurrence of spread-F traces measured by the Norfolk Island ionosonde span local times (LT) 21:15-01:30. At Townsville, the TIDs are first observed close to 7 UT (17 LT) and bring with them batches of Spread-F. The Spread-F then intensifies close to 11:24 UT (21:24 LT) and remains strong until 15 UT (1:00 LT), before finally ceasing at 17:30 UT (03:30 LT).

Next, the GPS data from receivers close to the Norfolk Island and Townsville ionosonde stations are examined as initial examples of the features and trends present throughout the GPS data. Figure 3 shows the observed vertical TEC (VTEC, upper panels) and the rate of TEC index (ROTI, lower panels) observed by the Norfolk Island (NORF, left) and Townsville (TOW2, right) GPS receivers on January 15, 2022. The VTEC data for both stations show the presence of TIDs that disrupt the diurnal pattern starting at $\sim$ 6 and 7 UT for NORF and TOW2, respectively, in good agreement with the ionosonde observations in Fig. 2. In the NORF data, the TIDs are observed in the individual satellite traces as rather small-amplitude wave structures compared to the variations over the 24-hour period. Slight differences in the timings of these structures (or phase progression) for different satellite links are due to the geographical spread of the ionospheric pierce points and the motion of the TIDs over the station. In the TOW2 data, the TIDs are much clearer as strong changes in VTEC for specific satellite links at different times. The phase progression of the VTEC structures overhead are much clearer in the TOW2 data. The lower panels reveal the times in which increased ROTI values were observed. For Norfolk Island (Fig. 3c) ROTI increases shortly after the TIDs arrive and then decreases back to low levels by 9 UT. Townsville also observed increased ROTI values once the main TIDs arrived and remained high until $\sim$ 15 UT once the strong Spread-F ceases, c.f. Fig. 2.

Next, we illustrate how the Ginan PPP software achieves convergence, as defined here by a 3-D position error of less than 10 cm. Figure 4 shows six examples of PPP convergence on January 15, 2022 using data collected by the NORF (top row) and TOW2 (bottom row) receivers. Each panel represents a ‘cold start’ of the PPP algorithm starting at a different time; 02:30 UT, 04:30 UT and 06:30 UT, as indicated in the subfigure titles. The positioning error was calculated as the difference between the PPP estimations and the known geodetic station locations. The position errors in the X, Y, and Z directions, as well as the full 3-D position, are shown in each panel. The 10 cm position error threshold is indicated by the dash-dot line, and zero error is indicated by the dashed line. Also displayed in each panel is the time it took for the 3-D position error to reach below 10 cm, indicated by the vertical dotted line; i.e., the convergence time.

Given the TID and subsequent Spread-F activity shown in the ionosonde data in Fig. 2, one might expect that PPP errors for nearby GPS receivers would noticeably increase during these periods. However, Fig. 4a shows that despite the onset of TIDs at approx. 6 UT for the NORF station, the position error remained below the 10-cm threshold. The same is true in Fig. 4d for the TOW2 station, for which the onset of TIDs was approx. 7 UT. While Fig. 4b shows that the NORF station position error increased following the commencement of Spread-F close to 9 UT, it remained well below 10 cm. Interestingly, despite the commencement of rather strong Spread-F at 11:24 UT at TOW2, Fig. 4f shows no significant increase in the position error. This is likely the result of running the PPP algorithm in ‘static mode’. From these results, one can conclude that the static-mode PPP algorithm was robust enough to remain at cm-level accuracy for these stations throughout the turbulent ionospheric conditions caused by the Tonga eruption, provided that convergence had already been achieved.

Figure 4 also illustrates how the convergence time is dependent on the start time of the algorithm. For the NORF station, the convergence time ranges from less than 1 hour beginning at 04:30 UT (Fig. 4b) to almost 4 hours when started from 06:30 UT (Fig.

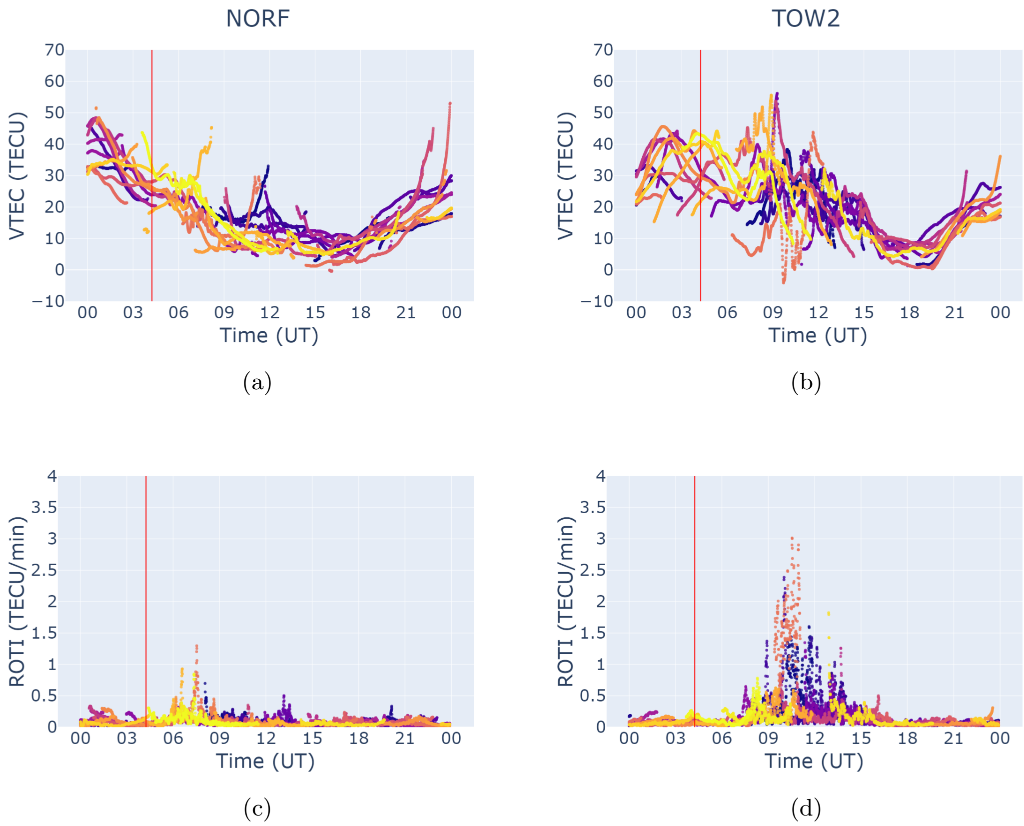


Figure 3: VTEC measured by (a) Norfolk Is. (NORF) and (b) Townsville (TOW2) GPS receivers with the different colors representing different satellite-to-ground links on January 15, 2022. The corresponding ROTI values for (c) NORF and (d) TOW2 stations. The red vertical lines indicate the time of the eruption.

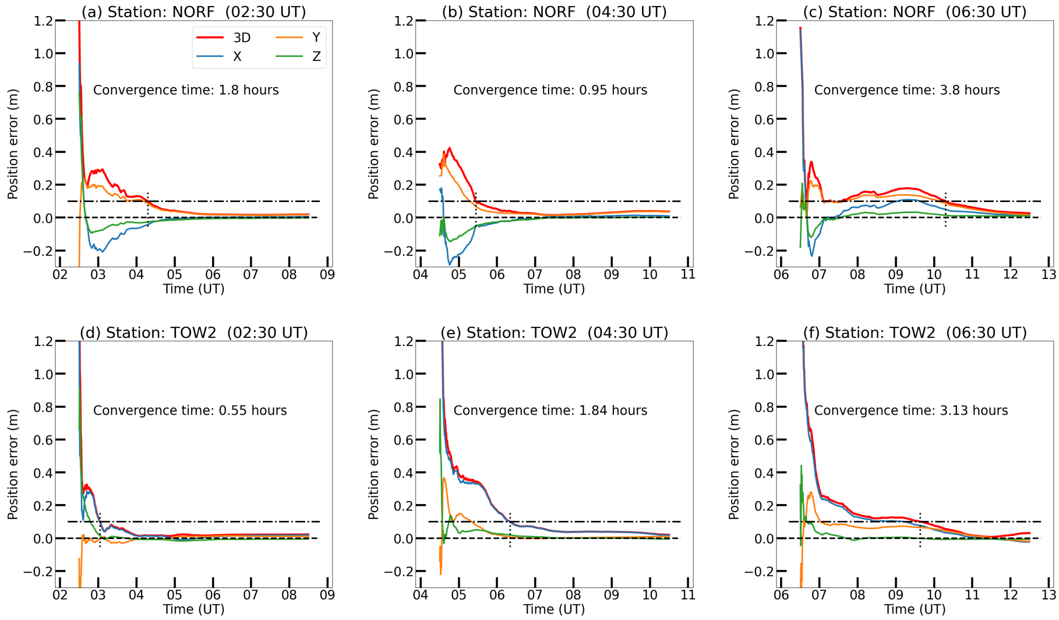


Figure 4: Examples of PPP convergence from a cold start using GPS data from the NORF (top row) and TOW2 (bottom row) commencing at 02:30 UT (left column), 04:30 UT (centre column) and 06:30 UT (right column) on January 15, 2022. Shown in each panel is the positioning error in X, Y and Z coordinates, in addition to the full 3-D position error. The dashed and dot-dashed horizon lines indicate position errors of 0 m and 10 cm, respectively. The moment when convergence was achieved and the associated convergence time are indicated in each panel by the vertical dotted lines and the text, respectively.

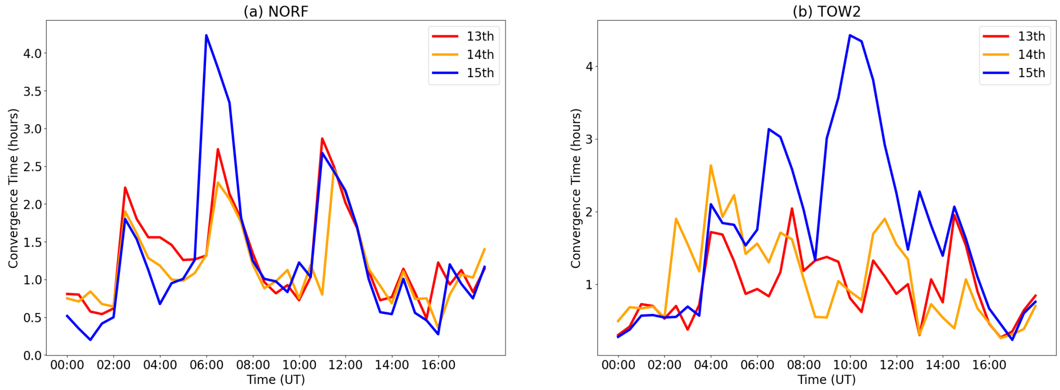


Figure 5: Diurnal variations in the PPP convergence time for the (a) NORF and (b) TOW2 GPS stations on the 13th, 14th and 15th of January, 2022.

4c). The TOW2 station shows a similar level of variation, ranging from 30 mins when started from 02:30 UT (Fig. 4d) up to more than 3 hours when started from 06:30 UT (Fig. 4c), which is $\sim$ 30 mins before the eruption effects reached Townsville. These results suggest a possible connection between the variable ionosphere in the wake of the eruption and the PPP convergence times at Norfolk Island and Townsville.

The PPP convergence time is a complicated parameter that is dependent on the number and geometry of available satellites, and the ability of the algorithm to model and account for the signal errors including the atmospheric components caused by the ionosphere and troposphere (e.g., Zumberge et al., 1997; Leick et al., 2015; Choy et al., 2017; Kouba et al., 2017; Teunissen & Montenbruck, 2017). To further explore the possible impact of the disturbed ionosphere on the PPP convergence time, a numerical experiment was performed using the GPS CORS across the Australian region. The Ginan software was used to perform the PPP processing using data from staggered start times throughout January 13-15, 2022, in 30-min steps. In other words, the experiment simulated a series of 'cold starts' of the PPP algorithm every 30-mins during January 13-15, 2022. At each time and for each station, the time it took for the PPP algorithm to achieve convergence was recorded. Figure 5 shows how the convergence time for the NORF (a) and TOW2 (b) stations varied throughout January 13-15. For January 13 and 14, convergence times for both stations were typically on the order of 30 mins to 2.5 hours, and appear to follow a similar diurnal variation for each station. On January 15, however, the convergence times are typically 2-4.5 hours, with some times showing significant differences compared to the January 13 and 14 values; particularly close to 6 UT for NORF and between 6 and 12 UT for TOW2. For NORF, the maximum increase in convergence time on January 15 (relative to January 14) was almost 3 hours at 6 UT. For TOW2, the maximum increase in convergence time was 3.6 hours at 10:30 UT.

In order to investigate what impact, if any, the disturbed ionosphere had on GPS PPP convergence time across the region, a reliable baseline was needed. At first glance of Fig. 5, it appears that simply choosing the PPP convergence time from the day prior as the baseline is a good option. However, some GPS stations showed significant differences between the diurnal variations in the convergence times between January 13 and 14; not shown here. In these cases, it is possible that the differences could be explained by a difference in the handling of the tropospheric delays by the algorithm, as the geomagnetic activity level was quiet and the satellite geometry was very similar. Therefore, in order to exclude times and GPS stations' data for which the chosen baseline of January 14 was not reliable, a simple selection criterion was used. Namely, if the con-

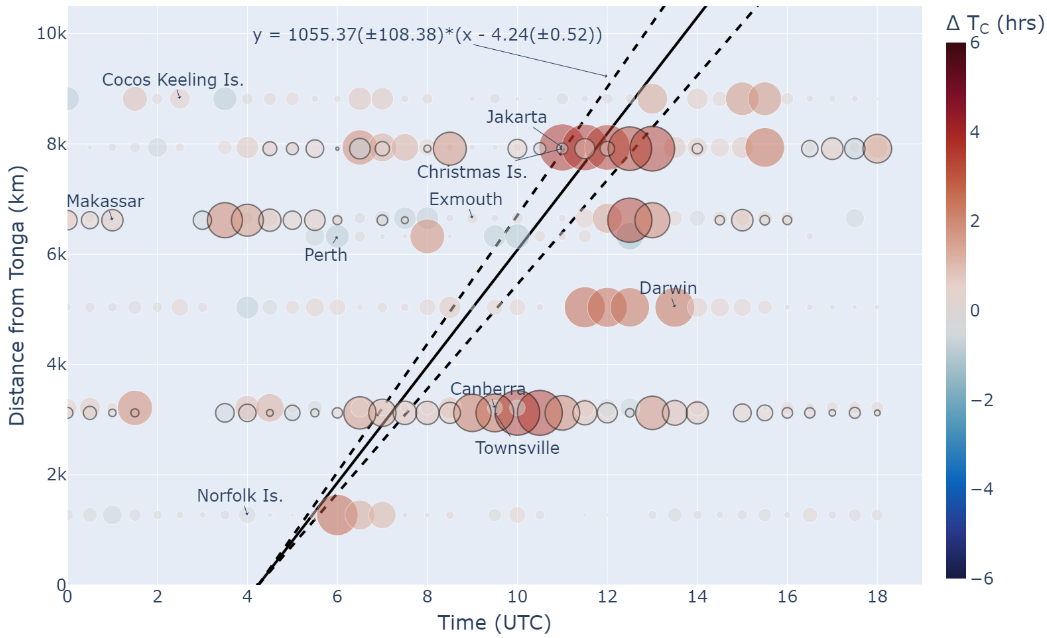


Figure 6: Distance from Tonga versus time colored according to the change in PPP convergence time, $\Delta T_C$, as determined using GPS stations located near the ionosonde stations in Figure 1, and two additional stations located at Makassar and Jakarta. The size of the circles also indicates the $\Delta T_C$ value. For reference, the trend line representing the propagation of the ionospheric disturbances as identified in the ionosonde data in Fig. 2 is shown. Due to some stations' data overlapping in the plot, Townsville, Makassar and Christmas Island data points are shown with black outlines.

vergence time for a given moment in the day of January 14 was different compared to January 13 by more than 1 hour, then that time was considered as a 'null' data point. Otherwise, the difference between the convergence time on January 15 and January 14 for that time of day was taken as the change in convergence time due to the disturbed ionosphere on the day of the Tonga volcano eruption, $\Delta T_C$.

Figure 6 shows how the change in convergence time varied throughout January 15 for GPS stations colocated with the ionosondes in Fig. 1, with two additional stations at farther distances; Makassar and Jakata in Indonesia. The size and color of the dots indicates the change in convergence time, $\Delta T_C$. Also plotted is the line of best fit that describes the propagation of the TIDs as detected by the ionosondes from Pradipta et al. (2023).

Firstly, it is worth mentioning that prior to the arrival of the TIDs, some GPS stations in Fig. 6 show some isolated increases in the convergence time on January 15 compared to January 14. Makassar, Christmas Island, Canberra and Perth all show isolated increases in the convergence time on the order of 2 hours before any ionospheric disturbances from the eruption arrive. However, most of the stations in Fig. 6 show significant and lasting convergence time increases after the TIDs arrive at their respective locations. There are the exceptions of Canberra, Exmouth and Perth that do not observe any clear convergence time increases. Interestingly, some GPS stations show convergence time increases the moment the TIDs arrive, for example Norfolk Island and Jakarta, whereas others observe their largest increases some hours later, for instance Darwin and Townsville.

In the Townsville ionosonde data shown in Fig. 2, it was noted that spread-F traces accompanied the arrival of TIDs at 7 UT (17 LT), with strong spread-F traces observed during 11:24-15:00 UT (21:15-01:00 LT). It is interesting to note that the largest $\Delta T_C$ increases for the TOW2/Townsville GPS station occurred for the algorithm start time of 10:30 UT (20:30 LT), consistent with the beginning of the 3.5-hour period of strong Spread-F activity detected by the Townsville ionosonde. Finally, it is also worth noting that the magnitude of the $\Delta T_C$ increases vary between the stations, from an increase of 2 hours observed at the Cocos Keeling Islands to an increase of 3.6 hours observed at Townsville and 3.8 hours at Jakarta.

To further explore the impact of the disturbed ionosphere on the GPS PPP convergence time across the region, Fig. 7 shows $\Delta T_C$ for all of the GPS stations each hour between 6 UT and 15 UT on January 15. At 6 and 7 UT, it can be seen that $\Delta T_C$ values were mostly close to 0; some stations across South Eastern Australia show some elevated values at 6 UT, but most reduce to 0 by 7 UT. At 6 UT, the Norfolk Island station – located to the southwest of Tonga approximately halfway to Australia – is already showing elevated convergence times, as also shown in Fig. 6. By 8 UT, some stations on Australia's northeastern coast are showing some elevated convergence times, which further increase at 9 UT. At this time, several stations show convergence time increases of more than 5 hours. At 10 UT, the convergence time increases in the far-north Australian region begin to decline as stations further south begin to show increases that reach 4 hours for some stations. The $\Delta T_C$ values are still elevated at 11 UT in the east Australian region, but some stations farther north and to the west are showing values close to 5 hours. At 12 UT, the elevated $\Delta T_C$ values across Australia's north and across Southeast Asia remain at 3-4 hours as the eastern Australian stations approach 0. There is a slight increase in $\Delta T_C$ across Australia's northeast once again at 13 UT to more than 3 hours, before almost all stations across the region approach $\Delta T_C = 0$ by 15 UT. An interactive map showing these data is included in the Supplementary Materials (S1).

In an effort to diagnose the physical phenomena that may be responsible for these impacts on PPP convergence, ionospheric observations made by these GPS stations are examined next. Figure 8 is the similar to Fig. 6, but the data points are colored according to the maximum ROTI value detected for each GPS station in each 30-min interval. Similar to the increased convergence times in Fig. 6, the ROTI values for most stations show a marked increase following the arrival of the TIDs from the volcano. Some stations observed increased ROTI values some time after the primary TID arrivals, such as Norfolk Island, Townsville and Darwin. The Perth and Exmouth stations generally show very low ROTI values, as does the Canberra station; although at 08:30 UT, Canberra shows one elevated ROTI value. The agreement between the ROTI results in Fig. 8 and the convergence time results in Fig. 6 suggests a strong link between the two.

To explore the potential link between ROTI and PPP convergence time, Figure 9 is similar to Fig. 7 but shows the 30-min maximum ROTI value for each GPS receiver; the full interactive map is available in the Supplementary Materials (S2). These maps show a lot of similar trends to those in Fig. 7, particularly the increased ROTI values over the northern Australian region compared to the south, and the increased values going into the Southeast Asian region. However, there is one notable difference between Figs. 7 and 9; namely panel (d) that corresponds to 9 UT. While the change in convergence times were low throughout South Eastern Australia, the ROTI values in Fig. 9 show that ROTI was actually quite high across this region. While the wave of increased ROTI clearly sweeps across northern Australia, the increased ROTI across southern parts of the country disappeared in place and did not make it to Western Australia.

Finally, VTEC observations made by the GPS stations are presented. Figure 10 is a series of maps of the 15-min averaged VTEC (i.e., $\langle VTEC \rangle$) for a select group of GPS stations at latitudes between 24°S and 10°S and longitudes between 128°E and 152°E (geographic). Each point represents the ionospheric pierce point (IPP) assuming an al-

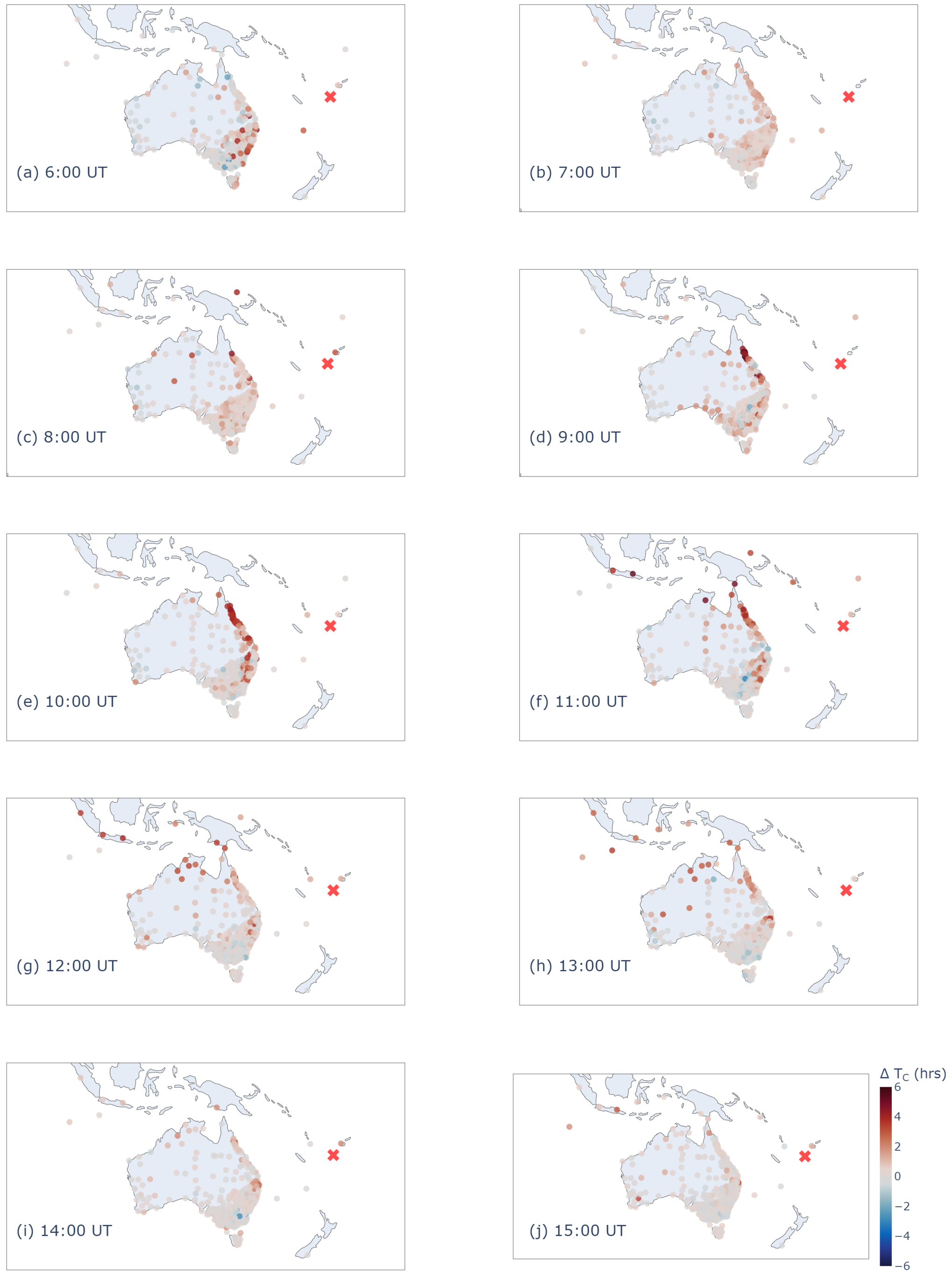


Figure 7: The change in PPP convergence time for GPS stations across the Australian/Southeast Asian region from (a) 6 UT until (j) 15 UT. The red cross indicates the location of Tonga. The full interactive map is included in the Supplementary Material S1.

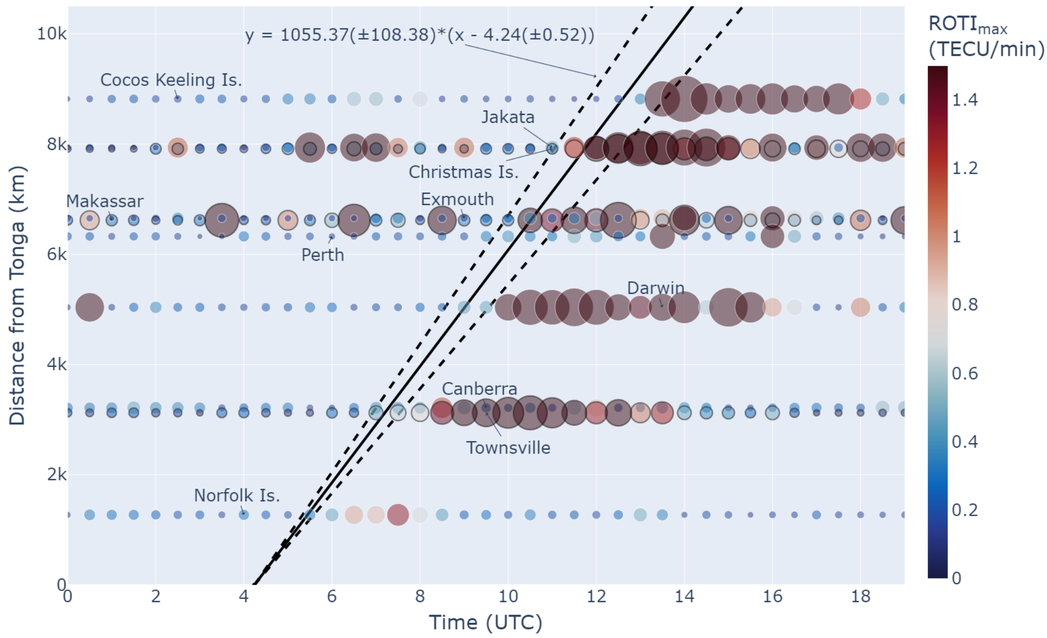


Figure 8: Same as Fig. 6, but colored according to the maximum ROTI observed for each station in every 30-min interval. Once again, Townsville, Makassar and Christmas Island data points are shown with black outlines.

titude of 400 km. A full interactive animation of this data sequence is included in the Supplementary Materials (S3). Figure 10a shows the presence of a deep $\langle VTEC \rangle$ valley over eastern of Papua New Guinea at 9 UT. By 09:30 UT (Fig. 10b) it appears as though the $\langle VTEC \rangle$ valley/depletion extends south to the Townsville station, and remains almost in place for the remaining times plotted. The shape of the $\langle VTEC \rangle$ depletion is quite pronounced in Fig. 10e (11 UT) as a thin dark blue feature with a north-south alignment. Within this depletion, values as low as 6 TECU were observed, and were as high as 48 TECU only 300 km to the west.

To track and measure the propagation of this $\langle VTEC \rangle$ depletion feature, Figure. 11 shows the same data from Fig. 10, but it is restricted to spanning latitudes 17°S–14°S and longitudes 140°E–155°E; i.e., the blue box in 10c. The depletion noted in Fig. 10 is quite clear in Fig. 11, along with some other $\langle VTEC \rangle$ variations during this interval. Fig. 11 also includes a manually plotted trendline that highlights the propagation of the most pronounced depletion with longitude; $y = 0.942x + 135.78$. A noteworthy observation is that this ionospheric depletion is propagating to the east, albeit rather slowly. As the trendline indicates, the depletion is propagating eastwards with a speed of $\sim 0.9$ °/h, or equivalently $\sim 30$ m/s (assuming 111 km/°).

## 4 Discussion

In the results above, the ionospheric variability resulting from the Hunga Tonga Volcano eruption across the Australian region was presented, followed by an investigation of the associated impact on PPP accuracy and convergence time. It was found that positioning accuracy did not appear to be adversely impacted in the wake of the eruption. Although, an experiment simulating 'cold starts' to the PPP algorithm showed that convergence times were affected by the variable ionosphere in the wake of the eruption.

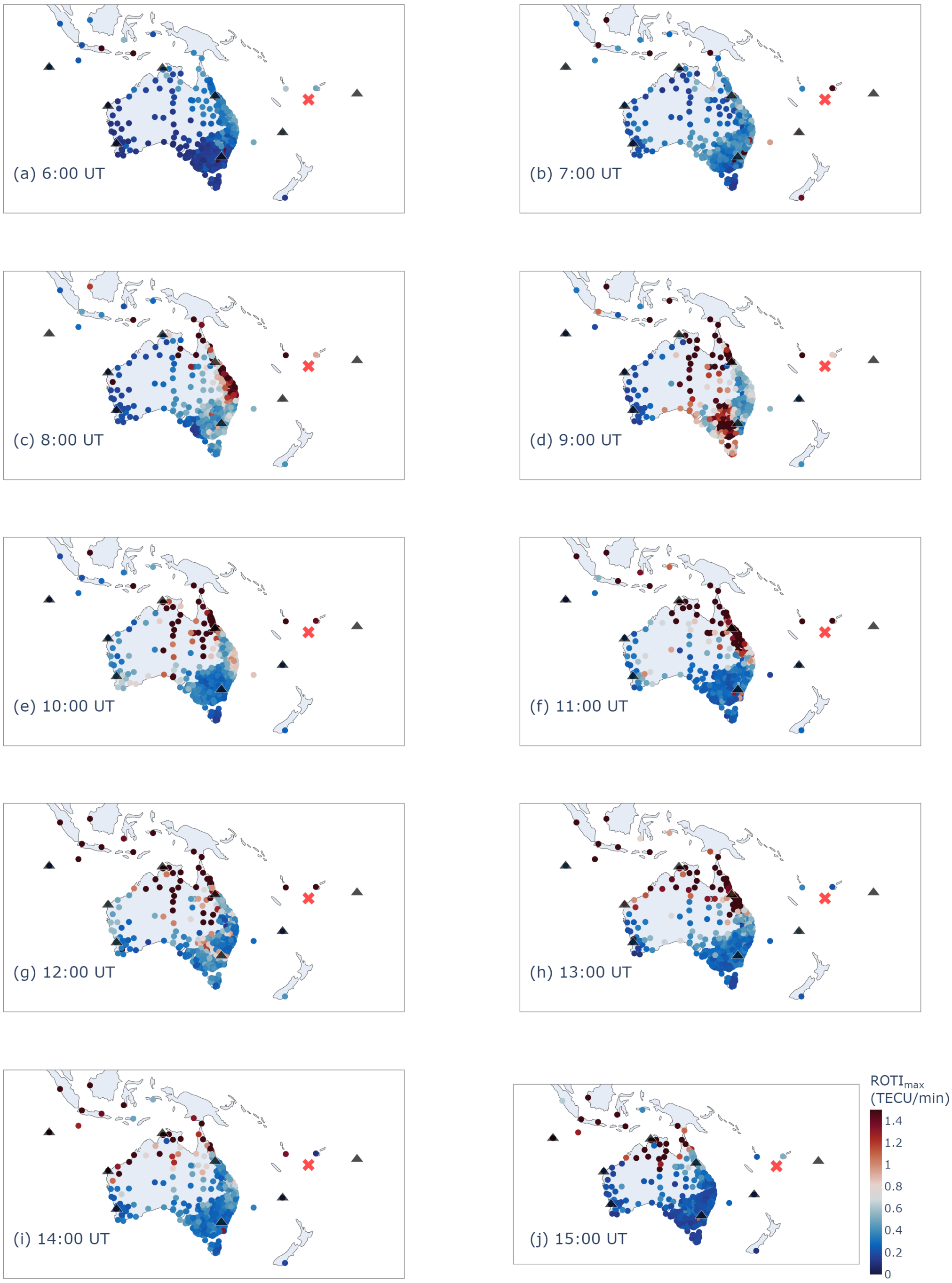


Figure 9: Same as Fig. 7, but showing the observed ROTI maximum in the 30-min following each time; i.e., panel a displays the maximum ROTI observed by each station between 6 and 6:30 UT. The full interactive map is included in the Supplementary Material S2.

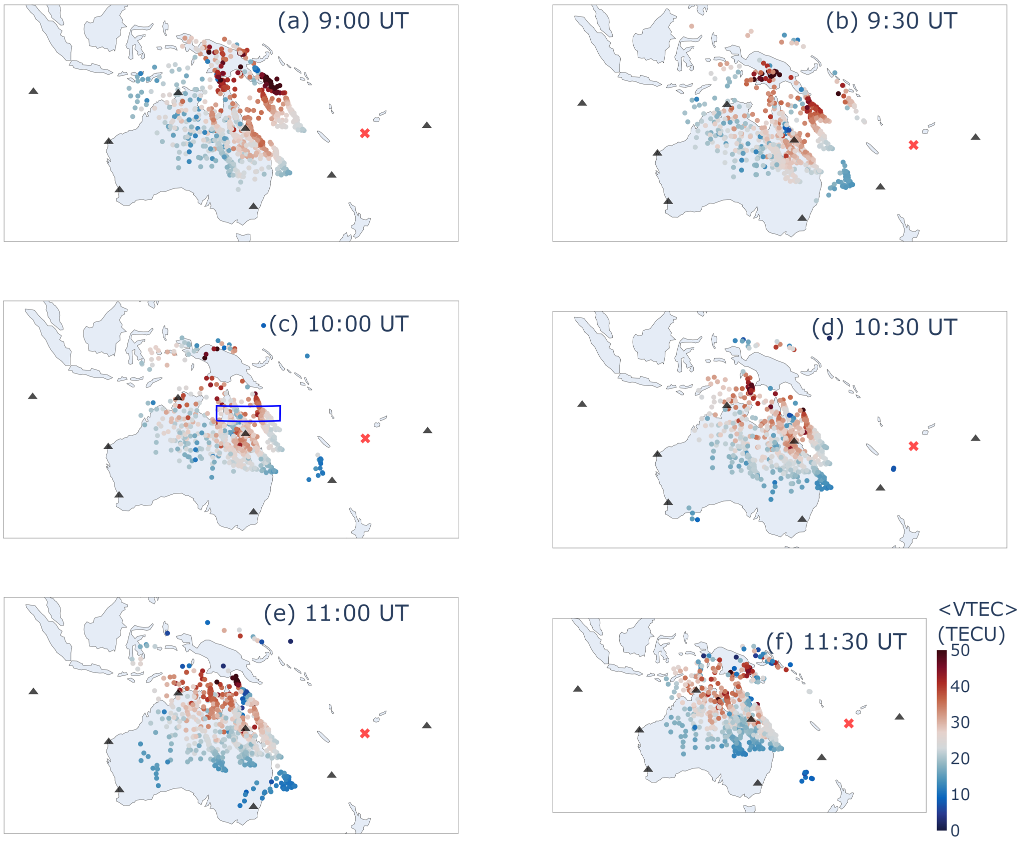


Figure 10: Maps showing the 15-min averaged VTEC (i.e., $\langle VTEC \rangle$) from 9 UT to 11:30 UT on January 15, 2022 for stations located between latitudes 24°S and 10°S and longitudes 128°E and 152°E (geographic). The blue box in panel (c) shows the range of latitudes and longitudes considered in the analysis to follow. The full interactive map is included in the Supplementary Material S3.

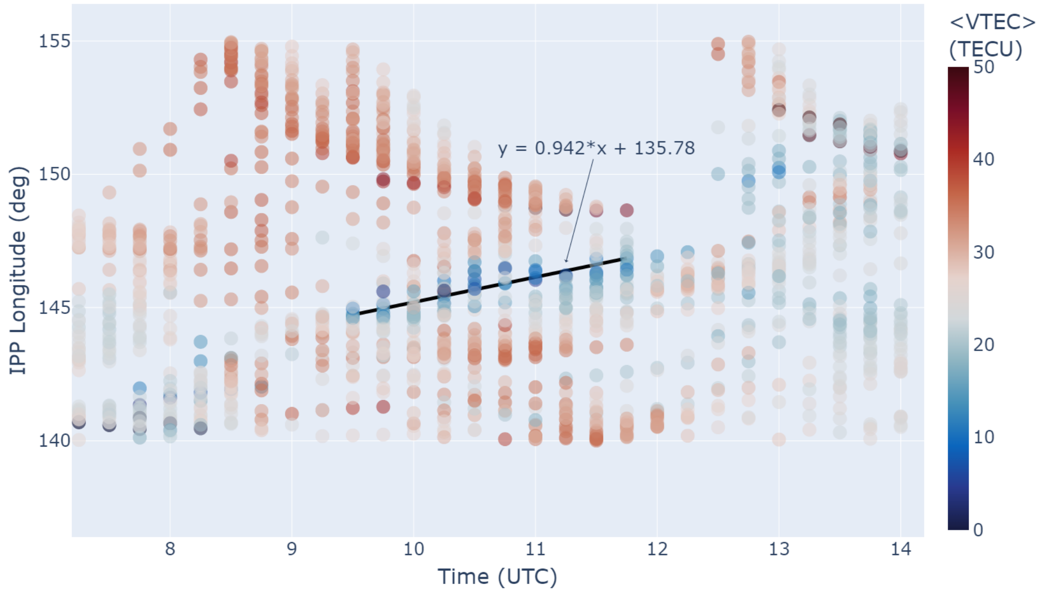


Figure 11: Ionospheric pierce point longitude versus time for data points for locations within the blue box in Fig. 10c – latitudes 17°S–14°S and longitudes 140°E–155°E – colored according to $\langle VTEC \rangle$.

Using the PPP convergence times from 13 and 14 January as a baseline, it was found that stations across northern Australia and Southeast Asia experienced significant convergence time increases on January 15, with some stations experiencing increases of more than 5 hours. It was revealed that the stations experiencing the largest convergence time increases measured extended periods of enhanced ROTI values. Examination of the 15-min averaged VTEC data then revealed the presence of a significant depletion that extended from Papua New Guinea into central eastern Queensland. A close examination of this depletion revealed that it was propagating eastwards with a velocity of $\sim$ 30 m/s.

PPP accuracy is at the core of PPP as a usable application. As such, previous works that have studied the impact of adverse ionospheric conditions on positioning focus on the solution accuracy, and this has typically been done using 'kinematic' mode. For instance, Poniatowski and Nykiel (2020) reported the degradation of PPP accuracy across central Europe during the 2015 St. Patrick's Day storm, with root mean square errors of 0.58m, 0.37m and 0.26m in the vertical, north and east directions, respectively. Z. Yang et al. (2020) also investigated the impact of the 2015 St. Patrick's Day storm on PPP accuracy, but their analysis included stations located around the world. They found that intense auroral activity played a significant role in degrading the PPP solutions, with $\sim$ 70% of high-latitude stations suffering position errors of greater than 1 m. Importantly, the most severe degradations in position accuracy were found to coincide with intense ionospheric irregularities, as determined by the GPS ROTI parameter. Z. Yang et al. (2020) also attributed some observed position accuracy degradation in low latitudes to large-scale TIDs – $\sim$ 1 TECU in amplitude – that were generated by the storm. In the present study, the PPP errors during the passage of the TIDs from the volcano eruption – and the subsequent Spread-F activity – appeared to be smaller compared to that reported by Z. Yang et al. (2020), despite the larger amplitude of the initial TIDs for this event, $\sim$ 3 TECU (S.-R. Zhang et al., 2022). A similar analysis of the 2017 September geomagnetic storms also revealed a strong relationship between enhanced ROTI and de-graded PPP accuracy (Zakharenkova & Cherniak, 2021). In their analysis, it was found that the 3-D errors rose to several meters due to the presence of small-scale ionospheric irregularities. The lower errors in the present study can be understood by the fact that 'static mode' was used in the positioning algorithm; i.e., the range of potential receiver velocities passed to the filter via the 'process noise' parameter was set to zero. Interestingly, the positioning errors in this study remained lower than 10 cm, provided that the solution had already converged. One exception is shown in Fig. 5c, where the arrival of TIDs at NORF delayed the convergence by $\sim 2$ hours. While Figure 5 only shows a few examples for two stations, their results largely reflect the results of the other stations considered in this analysis. Given the rather minimal impact of the volcano eruption on static-mode PPP accuracy across the Australian region, the focus of this study shifted to the potential impact on the PPP convergence time, which is a key limiting factor in the widespread use of PPP (Choy et al., 2017).

Here, the investigation into the PPP convergence time made use of an experiment in which 'cold starts' to the positioning algorithm were performed every 30-min during January 15, 2022. Perhaps the most significant finding in this study is that the change in convergence time – i.e., the difference between the 15th and 14th – reached 5 hours or higher for some stations. Interestingly, these convergence time increases were consistently observed over northern Australia, and were largely absent across central and southern Australia, c.f. Figs. 6 and 7.

At first glance, the ionosonde data showed several inconsistencies with the PPP convergence time results. All ionosonde stations observed clear TIDs associated with the volcano eruption, followed by some period of Spread-F activity in the ionograms. As reported by Pradipta et al. (2023), the propagation of the disturbances in these ionosonde data agrees well with other studies that have investigated the TID propagation using GPS TEC data (e.g., Themens et al., 2022; S.-R. Zhang et al., 2022). As observed by most ionosonde stations, the TIDs immediately gave way to Spread-F activity, but in some cases there was a significant delay between the arrival of the TIDs and the onset of Spread-F. For example, the Townsville station TVL5F, Fig. 2d, showed Spread-F activity commencing some 3 hrs after the initial TIDs passed, and the Learmonth station showed Spread-F commencing more than 6 hours after the TID passage. The intensity of the Spread-F also widely varied across the stations. Stations like Canberra, Townsville and Cocos Keeling Islands observed quite strong and prolonged Spread-F, whereas one of the stations closest to the eruption, Norfolk Island, and another among the farthest away, Perth, observed relatively weak Spread-F activity.

To better understand the differences in the detection of Spread-F across the Australian region, it helps to be reminded about what the presence of TID signatures and Spread-F in the ionograms indicates about the ionospheric plasma. The TID signatures highlighted in Fig. 2 that are characterized by descending traces are clear signatures of large-scale TIDs, on the order of 100s of kms (e.g., Cervera & Harris, 2014; Pederick et al., 2017). While Spread-F observed at low latitudes is typically associated with EPBs generated by the Generalized Rayleigh-Taylor instability during the post-sunset to local midnight hours (Sultan, 1996; Burke et al., 2004; Kelley et al., 2006; Carter et al., 2014, 2020, and references therein), mid-latitude Spread-F is generally considered to be due to the Perkins instability (e.g., Perkins, 1973; Kelley & Fukao, 1991) or specular reflections from medium-scale TIDs with scales on the order of 10s of kms (e.g., G. Bowman, 1981; G. G. Bowman & Monro, 1988; G. G. Bowman, 1990). Interestingly, the results in Fig. 6 do not appear to show a clear and consistent relationship between the presence of large-scale TIDs or medium-scale TIDs/spread F and increased PPP convergence times.

The GPS stations used in this study are not high-rate receivers that enable a detailed analysis into the full spectrum of ionospheric waves (e.g., Cervera & Thomas, 2006; van de Kamp & Cannon, 2009; Carrano et al., 2012). However, given the apparent motion of the GPS satellites above ground-based receivers and assuming typical ionospheric wave phase speeds, the GPS ROTI parameter can provide insight into the presence of ionospheric irregularities on the order of a few kms (e.g., Pi et al., 1997; Ma & Maruyama, 2006; Nishioka et al., 2008; Zou & Wang, 2009). Generally speaking, there is quite good agreement between the impact on the convergence time and enhanced ROTI, by comparing Figs. 6 and 8 and comparing Figs. 7 and 9. Although, one noted difference was the presence of enhanced ROTI that propagated over southeast Australia and then disappeared. The propagation of this ROTI disturbance agrees well with the propagation of the Lamb wave across the region reported by Aa et al. (2022) (see their Fig. 4). From these observations, one can conclude that the large-scale TIDs caused by the eruption had secondary small-scale irregularity generation all the way down to the scale of kms, making them detectable using the ROTI parameter. Although, an open question that arises is why did these secondary waves not continue to propagate across southern Australia? In other words, what caused the small-scale irregularities over southeast Australia at 9 UT in Fig. 9d to either no longer be generated – or be more heavily damped – by 10 UT in Fig. 9e, when the presence of the Lamb wave in the ROTI data was still clear over northern Australia? The answer either lies in the differences in the effectiveness of the energy cascade from large-scale to small-scale waves, or in the factors that control the damping of small-scale structures between northern and southern Australia. In either case, this is one interesting observation that requires further study and explanation.

In terms of the impact of ionospheric irregularities on the PPP convergence time, these results suggest that increased ROTI – and therefore the presence of small-scale (i.e., km-scale) ionospheric irregularities – tends to prolong PPP convergence times only in the event that the period of increased ROTI lasts for 30 mins or longer. This likely explains why stations in Australia's northern region are clearly impacted compared to the stations in southern and central Australia in Fig. 7. Therefore, an ongoing challenge for the GPS PPP community is to effectively mitigate the adverse impacts of extended periods of small-scale ionospheric irregularity activity.

The next question is by what physical mechanism are these small-scale ionospheric irregularities being generated in order to have such a detrimental impact on GPS PPP? At first glance, the most heavily influenced region in northeastern Australia are too far south for typical EPBs to be an obvious likely candidate. At 400 km above Townsville (i.e., the IPP), the magnetic latitude is 31.5°S, and the magnetic field line from this location maps to the equator at an altitude close to 2100 km; using a combination of the International Geomagnetic Reference Field (Maus et al., 2005; IAGA, 2010) and the Altitude Adjustment Corrected Geomagnetic (AACGM) (Baker & Wing, 1989; Laundal & Richmond, 2017) models. While some observations have been reported of such EPBs in the past (Ma & Maruyama, 2006; Cherniak & Zakharenkova, 2016), disturbances this large are particularly uncommon. Further, EPBs in the Southeast Asian/Australian longitude sector are not commonly observed during the months surrounding the December solstice (e.g., Burke et al., 2004; Nishioka et al., 2008; E. Dao et al., 2011; Carter et al., 2014, 2020). However, Aa et al. (2022) and Rajesh et al. (2022) recently reported observations of EPBs in the vicinity of Australia in the hours following the eruption. The detection of strong spread-F traces by the Townsville ionosonde coincides with local times that are typical of postsunset EPBs; i.e., 21-01 LT (see Fig. 2). Further, plots of VTEC in Fig. 10 in this study agree well with the observations reported by Rajesh et al. (2022) in revealing the presence of a deep depletion over northeastern Australia. Here, we measure that depletion to be 48 TECU on the ridges and 6 TECU in the valley. The propagation of this depletion was determined in this study to be eastwards (Fig. 11), on the order of 30 m/s. If this TEC depletion was a signature of TIDs propagating away from the eruption, then the propagation would have been westwards. Moreover, if it were TIDs from Tonga then the propagation would have been expected to much larger than 30 m/s. Such low eastward propagation speeds are typical of the F-region dynamo in the dusk sector, within which EPBs drift following their non-linear growth to the topside F region (e.g., Kelley, 2009; Chapagain et al., 2013, and references therein). Therefore, the local time of the Spread-F observed over Townsville, the VTEC depletion depth of 42 TECU and the associated eastward propagation speed in results presented here strongly indicate that the structure responsible for hours of increased ROTI, and subsequently increased PPP convergence times, in northeastern Australia is an EPB, in agreement with Rajesh et al. (2022).

It can be seen from the full animation of Fig. 11 (Supplementary Material (S3)) that data points associated with the depletion over northeastern Australia appeared as far south as 18°S, equivalent to 30°S magnetic latitude with an apex altitude of 1900 km over the magnetic equator. The authors are unaware of any other previously reported EPB disturbance that has been observed this far south over the Australian continent before, although similar-sized EPBs (referred to as 'super bubbles' due to their high altitude) have been reported using dense GPS stations across Japan (Ma & Maruyama, 2006). The EPBs that featured in that study would have also appeared over Australia due to magnetic conjugacy, but the relative sparsity of GPS stations across northern Australia did not allow clear EPB observations. However, the density of GPS stations across northern Australia has improved significantly during the solar cycle since Ma and Maruyama (2006)'s study. It is also worth highlighting that elements of Figs. 10 and 11 indicate the presence of TEC depletions farther to the south, but the sparsity of data at these locations makes a clear separation of TID disturbances from EPB-like disturbances difficult for this event. Further, the low density of GPS stations (and therefore, IPPs) across the rest of northern Australia makes a clear determination of whether depletions/EPBs were present difficult in this analysis. However, the impact on PPP convergence times across the rest of northern Australia and southeast Asia shown in Fig. 7 strongly suggests the ongoing presence of EPBs throughout the region during this event; a result in good agreement with the observations of Sun, Wenjie et al. (2022) and Aa et al. (2022) (in particular, the ICON plasma density depletions shown to the north of Australia in their Fig. 6). Some key insights into how TIDs from the eruption caused unseasonal EPB activity in the western Pacific sector can be gained from recent work by Huba et al. (2022). In Huba et al. (2022)'s modeling analysis, waves launched by the eruption caused significant perturbations in the zonal neutral wind in the equatorial plane, which effectively modified the equatorial upward plasma drift and gave rise to a huge EPB that spanned 30° in longitude (between 140-170°E). Huba et al. (2022) referred to this EPB as a 'super EPB' due to its large longitudinal extent. In addition, two very-high-altitude EPBs that reached 4000 km at $\sim$ 155°E and 180° were also generated by their simulation (altitudes well above those that Ma and Maruyama (2006) referred to as 'super bubbles' in their study). While the 30°-wide EPB in Huba et al. (2022)'s simulation was not clearly observed in the present study (possibly due to its limited latitudinal extent), the observation of a longitudinally narrow, high-altitude and low-density structure over northeastern Australia is consistent with the very-high-altitude EPBs in Huba et al. (2022)'s study; noting the rather reasonable differences in observed versus modeled location. This structure over northeastern Australia thus fits the definition of a 'super bubble' according to Ma and Maruyama (2006) and is in good agreement with the results of Rajesh et al. (2022). The impacts on GPS reported in the present study across the rest of northern Australia indicate that further analysis of this event farther towards the west across southern and southeastern Asia is needed.

## 5 Conclusions

The Hunga Tonga Volcano eruption is a unique and complicated event that has provided an unprecedented opportunity to study how the ionosphere couples to the lower atmosphere. In this study, the impact of the eruption – via the ionospheric disturbances that it generated – on GPS PPP was investigated. While static-mode PPP accuracy itself did not appear to be heavily affected, the time taken for convergence to be achieved was found to be significantly impacted. Across northern Australia the impact was particularly clear, with some GPS stations near Townsville reporting increases in convergence time of more than 5 hours. Long convergence times are limiting the widespread use of PPP, so the Hunga Tonga Volcano eruption presents a good opportunity to research the impacts and vulnerabilities of a variable ionosphere on PPP and to learn how to mitigate/account for them.

In this study, it was found that large- and medium-scale TIDs from the eruption were not the cause of convergence time increases, but it was the presence of small-scale ionospheric structures on the order of a few kms, as determined using the ROTI parameter. Further, it was revealed that PPP was robust enough to endure some enhanced ROTI, but not if the duration is longer than $\sim$ 30 mins. This observation effectively differentiated the impact observed on PPP in northern and southern Australia; northern Australia/southeast Asia experienced extended periods of increased ROTI and subsequently increased convergence times, whereas southern Australia only experienced a short burst of increased ROTI with marginal impact on convergence time.

The results of this study indicate that the ionospheric phenomenon responsible for the presence of small-scale irregularities in southern and northern Australia was different. In southern Australia, the small-scale irregularities were the result of secondary generation from the large- and medium-scale TIDs propagating away from the eruption. The enhanced ROTI region propagated to the west in a manner consistent with the Lamb waves previously reported. These small-scale structures were rather promptly damped and did not propagate far beyond southeastern Australia. In northern Australia, the extended periods of enhanced ROTI were found to be due to the presence of at least one 'super bubble' that was observed as far south as $\sim$30°S magnetic latitude, with an estimated apex altitude of $\sim$ 1900 km above the magnetic equator; this is the same 'super EPB' recently reported by Rajesh et al. (2022). The VTEC data revealed that the EPB was $\sim$ 42 TECU deep and $\sim$ 300 km across in longitude. Further, it was shown that the EPB traveled eastwards at $\sim$ 30 m/s, consistent with the F-region dynamo speed and direction. This super bubble is the largest/most southward-reaching EPB observed over the Australian continent; only recently made possible due to GPS station deployments in the region.

The Hunga Tonga Volcano eruption stands as an excellent example of how ionospheric variability can adversely influence satellite-based precise positioning that is increasingly heavily relied upon across many industries and sectors around the world.

## 6 Open Research

The Bureau of Meteorology Space Weather Services' World Data Centre provides ionosonde data via their website; https://www.sws.bom.gov.au/World_Data_Centre. Geoscience Australia provides GNSS data for all of the stations used in this analysis via their Global Navigation Satellite System Data Centre; https://gnss.ga.gov.au/. Geoscience Australia's Ginan platform is also accessible via their github repository; https://geoscienceaustralia.github.io/ginan/. The higher level analysis products, particularly the PPP convergence times that were calculated using Ginan, are available on the Zenodo data repository (doi:10.5281/zenodo.7694409).

**Acknowledgments**

B. A. Carter, S. Choy and T. Dao would like to acknowledge the support of FrontierSI (project PA1002A). M. Le Huy was supported by the Vietnam Academy of Science and Technology under the grant number NVCC 12.02/22-22. R. Pradipta's time was partially supported by grant FA9550-20-1-0313 from the Air Force Office of Scientific Research. The authors would also like to acknowledge the advice and assistance of R. Maj in running Geoscience Australia's Ginan platform.

## References

Aa, E., Zhang, S.-R., Erickson, P. J., Vierinen, J., Coster, A. J., Goncharenko, L. P., ... Rideout, W. (2022). Significant Ionospheric Hole and Equatorial Plasma Bubbles After the 2022 Tonga Volcano Eruption. *Space Weather*, *20*(7), e2022SW003101. doi: https://doi.org/10.1029/2022SW003101

Astafyeva, E., Maletckii, B., Mikesell, T. D., Munaibari, E., Ravanelli, M., Coisson, P., ... Rolland, L. (2022). The 15 January 2022 Hunga Tonga Eruption History as Inferred From Ionospheric Observations. *Geophysical Research Letters*, *49*(10), e2022GL098827. doi: https://doi.org/10.1029/2022GL098827

Baker, K. B., & Wing, S. (1989). A new magnetic coordinate system for conjugate studies at high latitudes. *Journal of Geophysical Research: Space Physics*, *94*(A7), 9139–9143. doi: https://doi.org/10.1029/JA094iA07p09139

Banville, S., Collins, P., Zhang, W., & Langley, R. B. (2014). Global and Regional Ionospheric Corrections for Faster PPP Convergence. *Navigation*, *61*(2), 115-124. doi: https://doi.org/10.1002/navi.57

Bisnath, S., & Gao, Y. (2009). Current state of precise point positioning and future prospects and limitations. In *Observing our changing earth* (pp. 615–623). Springer.

Borries, C., Jakowski, N., & Wilken, V. (2009). Storm induced large scale tids observed in gps derived tec. *Annales Geophysicae*, *27*(4), 1605–1612. doi: https://doi.org/10.5194/angeo-27-1605-2009

Bowman, G. (1981). The nature of ionospheric spread-F irregularities in mid-latitude regions. *Journal of Atmospheric and Terrestrial Physics*, *43*(1), 65-79. doi: https://doi.org/10.1016/0021-9169(81)90010-6

Bowman, G. G. (1990). A review of some recent work on mid-latitude spread-¡i¿f¡/i¿ occurrence as detected by ionosondes. *Journal of geomagnetism and geoelectricity*, *42*(2), 109-138. doi: https://doi.org/10.5636/jgg.42.109

Bowman, G. G., & Monro, P. E. (1988). Mid-latitude range spread and travelling ionospheric disturbances. *Journal of Atmospheric and Terrestrial Physics*, *50*(3), 215-223. doi: https://doi.org/10.1016/0021-9169(88)90070-0

Burke, W. J., Gentile, L. C., Huang, C. Y., Valladres, C. E., & Su, S. Y. (2004). Longitudinal variability of equatorial plasma bubbles observed by DMSP and ROCSAT-1. *J. Geophys. Res.*, *109*. (A12301) doi: https://doi.org/10.1029/2004JA010583

Carrano, C. S., Valladares, C. E., & Groves, K. M. (2012). Latitudinal and local time variation of ionospheric turbulence parameters during the conjugate point equatorial experiment in Brazil. *International Journal of Geophysics*, *2012*.

Carter, B. A., Currie, J. L., Dao, T., Yizengaw, E., Retterer, J., Terkildsen, M., ... Caton, R. (2020). On the Assessment of Daily Equatorial Plasma Bubble Occurrence Modeling and Forecasting. *Space Weather*, *18*(9), e2020SW002555. doi: https://doi.org/10.1029/2020SW002555

Carter, B. A., Ram, S. T., Yizengaw, E., Pradipta, R., Retterer, J., Norman, R., ... others (2018). Unseasonal development of post-sunset F-region irregularities over Southeast Asia on 28 July 2014: 1. Forcing from above? *Progress in Earth and Planetary Science*, *5*(1), 1–12.

Carter, B. A., Yizengaw, E., Retterer, J. M., Francis, M., Terkildsen, M., Marshall, R., ... Zhang, K. (2014). An analysis of the quiet-time day-to-day variability in the formation of post-sunset equatorial plasma bubbles in the Southeast Asian region. *J. Geophys. Res.*, *119*, 3206–3223. doi: https://doi.org/10.1002/2013JA019570

Carvajal, M., Sepúlveda, I., Gubler, A., & Garreaud, R. (2022). Worldwide signature of the 2022 tonga volcanic tsunami. *Geophysical Research Letters*, *49*(6), e2022GL098153. doi: https://doi.org/10.1029/2022GL098153

Cervera, M. A., & Harris, T. J. (2014). Modeling ionospheric disturbance features in quasi-vertically incident ionograms using 3-d magnetoionic ray tracing and atmospheric gravity waves. *Journal of Geophysical Research: Space Physics*, *119*(1), 431-440. doi: https://doi.org/10.1002/2013JA019247

Cervera, M. A., & Thomas, R. M. (2006). Latitudinal and temporal variation of equatorial ionospheric irregularities determined from GPS scintillation observations. *Annales Geophysicae*, *24*(12), 3329–3341. doi: https://doi.org/10.5194/angeo-24-3329-2006

Chapagain, N. P., Fisher, D. J., Meriwether, J. W., Chau, J. L., & Makela, J. J. (2013). Comparison of zonal neutral winds with equatorial plasma bubble and plasma drift velocities. *Journal of Geophysical Research: Space Physics*, *118*(4), 1802-1812. doi: https://doi.org/10.1002/jgra.50238

Cherniak, I., & Zakharenkova, I. (2016). First observations of super plasma bubbles in Europe. *Geophysical Research Letters*, *43*(21), 11,137-11,145. doi: https://doi.org/10.1002/2016GL071421

Choy, S., Bisnath, S., & Rizos, C. (2017). Uncovering common misconceptions in GNSS Precise Point Positioning and its future prospect. *GPS solutions*, *21*(1), 13–22.

Collins, P., & Bisnath, S. (2011). Issues in Ambiguity Resolution for Precise Point Positioning. In *Proceedings of the 24th international technical meeting of the satellite division of the institute of navigation (ion gnss 2011)* (pp. 679–687).

Collins, P., Lahaye, F., & Bisnath, S. (2012). External ionospheric constraints for improved PPP-AR initialisation and a generalised local augmentation concept. In *Proceedings of the 25th international technical meeting of the satellite division of the institute of navigation (ion gnss 2012)* (pp. 3055–3065).

Currie, J., Carter, B., Retterer, J., Dao, T., Pradipta, R., Caton, R., . . . others (2021). On the generation of an unseasonal EPB over South East Asia. *Journal of Geophysical Research: Space Physics*, *126*(2), e2020JA028724. doi: https://doi.org/10.1029/2020JA028724

Dao, E., Kelley, M. C., Roddy, P., Retterer, J., Ballenthin, J. O., de La Beaujardiere, O., & Su, Y.-J. (2011). Longitudinal and seasonal dependence of nighttime equatorial plasma density irregularities during solar minimum detected on the C/NOFS satellite. *Geophys. Res. Lett.*, *38*. doi: https://doi.org/10.1029/2011GL047046

Dao, T., Le Huy, M., Carter, B., Le, Q., Trinh, T. T., Phan, B. N., & Otsuka, Y. (2020). New observations of the total electron content and ionospheric scintillations over Ho Chi Minh City. *Science of the Earth*, *42*(4), 320–333. doi: 10.15625/0866-7187/42/4/15281

Díaz, J., & Rigby, S. (2022). Energetic output of the 2022 Hunga Tonga–Hunga Ha 'apai volcanic eruption from pressure measurements. *Shock Waves*, *32*(6), 553–561.

Duong, V. T. (2020). *Precise Point Positioning with ambiguity resolution using multi-frequency multi-constellation GNSS measurements* (PhD Thesis). RMIT University.

Geng, J., & Bock, Y. (2013). Triple-frequency GPS precise point positioning with rapid ambiguity resolution. *Journal of geodesy*, *87*, 449–460.

Ghent, J. N., & Crowell, B. W. (2022). Spectral Characteristics of Ionospheric Disturbances Over the Southwestern Pacific From the 15 January 2022 Tonga Eruption and Tsunami. *Geophysical Research Letters*, *49*(20), e2022GL100145. doi: https://doi.org/10.1029/2022GL100145

Harding, B. J., Wu, Y.-J. J., Alken, P., Yamazaki, Y., Triplett, C. C., Immel, T. J., . . . Xiong, C. (2022). Impacts of the January 2022 Tonga Volcanic Eruption on the Ionospheric Dynamo: ICON-MIGHTI and Swarm Observations of

Extreme Neutral Winds and Currents. *Geophysical Research Letters*, *49*(9), e2022GL098577. doi: https://doi.org/10.1029/2022GL098577

Hofmann-Wellenhof, B., Lichtenegger, H., & Wasle, E. (2007). *GNSS–Global Navigation Satellite Systems: GPS, GLONASS, Galileo, and more.* Springer Science & Business Media.

Hong, J., Kil, H., Lee, W. K., Kwak, Y.-S., Choi, B.-K., & Paxton, L. J. (2022). Detection of Different Properties of Ionospheric Perturbations in the Vicinity of the Korean Peninsula After the Hunga-Tonga Volcanic Eruption on 15 January 2022. *Geophysical Research Letters*, *49*(14), e2022GL099163. doi: https://doi.org/10.1029/2022GL099163

Huba, J., Becker, E., & Vadas, S. (2022). Simulation Study of the 15 January 2022 Tonga Event: Development of Super Equatorial Plasma Bubbles. *Geophysical Research Letters*, e2022GL101185. doi: https://doi.org/10.1029/2022GL101185

IAGA. (2010). *International Geomagnetic Reference Field - 11th Generation.* (NOAA National Centers for Environmental Information) doi: https://doi.org/10.7289/V58050JN

Johnston, G., Riddell, A., & Hausler, G. (2017). The international GNSS service. In *Springer handbook of global navigation satellite systems* (pp. 967–982). Springer.

Kelley, M. C. (2009). *The Earth's Ionosphere: Plasma Physics and Electrodynamics* (2nd ed.). Elsevier, London.

Kelley, M. C., & Fukao, S. (1991). Turbulent upwelling of the mid-latitude ionosphere: 2. Theoretical framework. *Journal of Geophysical Research: Space Physics*, *96*(A3), 3747-3753. doi: https://doi.org/10.1029/90JA02252

Kelley, M. C., Makela, J. J., & de La Beaujardiére, O. (2006). Convective ionospheric storms: A major space weather problem. *Space Weather*, *4*. doi: 10.1029/2005SW000144

Klobuchar, J. A. (1986). Design and characteristics of the GPS ionospheric time delay algorithm for single frequency users. In *Plans'86-position location and navigation symposium* (pp. 280–286).

Kotake, N., Otsuka, Y., Tsugawa, T., Ogawa, T., & Saito, A. (2006). Climatological study of gps total electron content variations caused by medium-scale traveling ionospheric disturbances. *Journal of Geophysical Research: Space Physics*, *111*(A4). doi: https://doi.org/10.1029/2005JA011418

Kouba, J., Lahaye, F., & Tétreault, P. (2017). Precise Point Positioning. In P. J. Teunissen & O. Montenbruck (Eds.), *Springer handbook of global navigation satellite systems* (pp. 723–751). Cham: Springer International Publishing. doi: https://doi.org/10.1007/978-3-319-42928-1_25

Laundal, K. M., & Richmond, A. D. (2017). Magnetic coordinate systems. *Space Science Reviews*, *206*(1-4), 27–59.

Lay, E. H., Parker, P. A., Light, M., Carrano, C. S., Debchoudhury, S., & Haaser, R. A. (2018). Midlatitude Ionospheric Irregularity Spectral Density as Determined by Ground-Based GPS Receiver Networks. *Journal of Geophysical Research: Space Physics*, *123*(6), 5055-5067. doi: https://doi.org/10.1029/2018JA025364

Le, G., Liu, G., Yizengaw, E., & Englert, C. R. (2022). Intense Equatorial Electrojet and Counter Electrojet Caused by the 15 January 2022 Tonga Volcanic Eruption: Space- and Ground-Based Observations. *Geophysical Research Letters*, *49*(11), e2022GL099002. doi: https://doi.org/10.1029/2022GL099002

Le Huy, M., Tran Thi, L., Fleury, R., Amory-Mazaudier, C., Le Truong, T., Nguyen Chien, T., & Nguyen Ha, T. (2016). TEC variations and ionospheric disturbances during the magnetic storm in March 2015 observed from continuous GPS data in the Southeast Asia region. *Vietnam Journal of Earth Sciences*, *38*(3), 287–305. doi: https://doi.org/10.15625/0866-7187/38/3/8714

Leick, A., Rapoport, L., & Tatarnikov, D. (2015). *GPS satellite surveying.* John Wiley & Sons.

Li, X., Zhang, X., Ren, X., Fritsche, M., Wickert, J., & Schuh, H. (2015). Precise positioning with current multi-constellation global navigation satellite systems: GPS, GLONASS, Galileo and BeiDou. *Scientific reports*, *5*(1), 1–14.

Luo, X., Du, J., Lou, Y., Gu, S., Yue, X., Liu, J., & Chen, B. (2022). A Method to Mitigate the Effects of Strong Geomagnetic Storm on GNSS Precise Point Positioning. *Space Weather*, *20*(1), e2021SW002908. doi: https://doi.org/10.1029/2021SW002908

Luo, X., Gu, S., Lou, Y., Xiong, C., Chen, B., & Jin, X. (2018). Assessing the Performance of GPS Precise Point Positioning Under Different Geomagnetic Storm Conditions during Solar Cycle 24. *Sensors*, *18*(6). doi: https://doi.org/10.3390/s18061784

Ma, G., & Maruyama, T. (2006). A super bubble detected by dense GPS network at east Asian longitudes. *Geophysical Research Letters*, *33*(21). doi: https://doi.org/10.1029/2006GL027512

Maletckii, B., & Astafyeva, E. (2022). Near-Real-Time Analysis of the Ionospheric Response to the 15 January 2022 Hunga Tonga-Hunga Ha'apai Volcanic Eruption. *Journal of Geophysical Research: Space Physics*, *127*(10), e2022JA030735. doi: https://doi.org/10.1029/2022JA030735

Mannucci, A., Wilson, B., Yuan, D., Ho, C., Lindqwister, U., & Runge, T. (1998). A global mapping technique for GPS-derived ionospheric total electron content measurements. *Radio science*, *33*(3), 565–582.

Matoza, R. S., Fee, D., Assink, J. D., Iezzi, A. M., Green, D. N., Kim, K., ... Wilson, D. C. (2022). Atmospheric waves and global seismoacoustic observations of the January 2022 Hunga eruption, Tonga. *Science*, *377*(6601), 95-100. doi: https://doi.org/10.1126/science.abo7063

Maus, S., Macmillan, S., Chernova, T., Choi, S., Dater, D., Golovkov, V., ... Zvereva, T. (2005). The 10th generation international geomagnetic reference field. *Phys. Earth Planet. Inter.*, *151*, 320-322.

Nishioka, M., Saito, A., & Tsugawa, T. (2008). Occurrence characteristics of plasma bubble derived from global ground-based GPS receiver networks. *J. Geophys. Res.*, *113*. (A05301) doi: 10.1029/2007JA012605

Odijk, D. (2002). Fast precise GPS positioning in the presence of ionospheric delays. *Publications on Geodesy, 52*.

Otsuka, Y., Ogawa, T., Saito, A., Tsugawa, T., Fukao, S., & Miyazaki, S. (2002). A new technique for mapping of total electron content using GPS network in Japan. *Earth, planets and space*, *54*(1), 63–70.

Pederick, L. H., Cervera, M. A., & Harris, T. J. (2017). Interpreting observations of large-scale traveling ionospheric disturbances by ionospheric sounders. *Journal of Geophysical Research: Space Physics*, *122*(12), 12,556-12,569. doi: https://doi.org/10.1002/2017JA024337

Perkins, F. (1973). Spread f and ionospheric currents. *Journal of Geophysical Research*, *78*(1), 218-226. doi: https://doi.org/10.1029/JA078i001p00218

Pi, X., Mannucci, A., Lindqwister, U., & Ho, C. (1997). Monitoring of global ionospheric irregularities using the worldwide GPS network. *Geophysical Research Letters*, *24*(18), 2283–2286.

Poniatowski, M., & Nykiel, G. (2020). Degradation of Kinematic PPP of GNSS Stations in Central Europe Caused by Medium-Scale Traveling Ionospheric Disturbances During the St. Patrick's Day 2015 Geomagnetic Storm. *Remote Sensing*, *12*(21). doi: https://doi.org/10.3390/rs12213582

Pradipta, R., Carter, B. A., Currie, J., Choy, S., Wilkinson, P., Maher, P., & Marshall, R. (2023). n the Propagation of Traveling Ionospheric Disturbances from the Hunga Tonga-Hunga Ha'apai Volcano Eruption and their Possible Connection with Tsunami Waves. *Geophysical Research Letters*, 2022GL101925, accepted 3-Mar-2023.

Pradipta, R., Valladares, C. E., Carter, B. A., & Doherty, P. H. (2016). Interhemispheric propagation and interactions of auroral traveling ionospheric disturbances near the equator. *Journal of Geophysical Research: Space Physics*, *121*(3), 2462-2474. doi: https://doi.org/10.1002/2015JA022043

Pradipta, R., Valladares, C. E., & Doherty, P. H. (2015). Ionosonde observations of ionospheric disturbances due to the 15 February 2013 Chelyabinsk meteor explosion. *Journal of Geophysical Research: Space Physics*, *120*(11), 9988-9997. doi: https://doi.org/10.1002/2015JA021767

Pyle, D. M. (2015). Sizes of volcanic eruptions. In *The encyclopedia of volcanoes* (pp. 257–264). Elsevier.

Pérez-Ruiz, M., de Santos, P. G., Ribeiro, A., Fernandez-Quintanilla, C., Peruzzi, A., Vieri, M., … Agüera, J. (2015). Highlights and preliminary results for autonomous crop protection. *Computers and Electronics in Agriculture*, *110*, 150-161. doi: https://doi.org/10.1016/j.compag.2014.11.010

Rajesh, P. K., Lin, C. C. H., Lin, J. T., Lin, C. Y., Liu, J. Y., Matsuo, T., … Tsai, H. F. (2022). Extreme Poleward Expanding Super Plasma Bubbles Over Asia-Pacific Region Triggered by Tonga Volcano Eruption During the Recovery-Phase of Geomagnetic Storm. *Geophysical Research Letters*, *49*(15), e2022GL099798. doi: https://doi.org/10.1029/2022GL099798

Rao, A. S., Radanovic, M., Liu, Y., Hu, S., Fang, Y., Khoshelham, K., … Ngo, T. (2022). Real-time monitoring of construction sites: Sensors, methods, and applications. *Automation in Construction*, *136*, 104099. doi: https://doi.org/10.1016/j.autcon.2021.104099

Sultan, P. J. (1996). Linear theory and modeling of the Rayleigh-Taylor instability leading to the occurrence of equatorial spread F. *J. Geophys. Res.*, *101*, 26875-26891.

Sun, Wenjie, Kaippallimyalil Kuriakose, Ajith, Li, Guozhu, Li, Yu, Zhao, Xiukuan, Hu, Lianhuan, … Liu, Libo (2022). Unseasonal super ionospheric plasma bubble and scintillations seeded by the 2022 Tonga Volcano Eruption related perturbations. *J. Space Weather Space Clim.*, *12*, 25. doi: https://doi.org/10.1051/swsc/2022024

Teunissen, P. J., & Montenbruck, O. (2017). *Springer handbook of global navigation satellite systems* (Vol. 10). Springer.

Themens, D. R., Watson, C., Žagar, N., Vasylkevych, S., Elvidge, S., McCaffrey, A., … Jayachandran, P. T. (2022). Global propagation of ionospheric disturbances associated with the 2022 tonga volcanic eruption. *Geophysical Research Letters*, *49*(7), e2022GL098158. doi: https://doi.org/10.1029/2022GL098158

Tsugawa, T., Saito, A., Otsuka, Y., Nishioka, M., Maruyama, T., Kato, H., … Murata, K. (2011). Ionospheric disturbances detected by GPS total electron content observation after the 2011 off the Pacific coast of Tohoku Earthquake. *Earth, planets and space*, *63*(7), 875–879.

Van Bree, R. J., Tiberius, C. C., & Hauschild, A. (2009). Real time satellite clocks in single frequency precise point positioning. In *Proceedings of the 22nd international technical meeting of the satellite division of the institute of navigation (ion gnss 2009)* (pp. 2400–2414).

van de Kamp, M. M. J. L., & Cannon, P. S. (2009). Spectra of equatorial total electron content derived from GPS signals. *Annales Geophysicae*, *27*(5), 2205–2214. doi: https://doi.org/10.5194/angeo-27-2205-2009

Vergoz, J., Hupe, P., Listowski, C., Le Pichon, A., Garcés, M., Marchetti, E., … Mialle, P. (2022). IMS observations of infrasound and acoustic-gravity waves produced by the January 2022 volcanic eruption of Hunga, Tonga: A global analysis. *Earth and Planetary Science Letters*, *591*, 117639. doi: https://doi.org/10.1016/j.epsl.2022.117639

Woodgate, P., Coppa, I., Choy, S., Phinn, S., Arnold, L., & Duckham, M. (2017).

The Australian approach to geospatial capabilities; positioning, earth observation, infrastructure and analytics: issues, trends and perspectives. *Geo-spatial information science*, *20*(2), 109–125.

Wright, C. J., Hindley, N. P., Alexander, M. J., Barlow, M., Hoffmann, L., Mitchell, C. N., ... Yue, J. (2022). Surface-to-space atmospheric waves from Hunga Tonga–Hunga Ha'apai eruption. *Nature*, *609*(7928), 741–746. doi: https://doi.org/10.1038/s41586-022-05012-5

Yang, H., Monte-Moreno, E., & Hernández-Pajares, M. (2017). Multi-TID detection and characterization in a dense Global Navigation Satellite System receiver network. *Journal of Geophysical Research: Space Physics*, *122*(9), 9554-9575. doi: https://doi.org/10.1002/2017JA023988

Yang, Z., Morton, Y. T. J., Zakharenkova, I., Cherniak, I., Song, S., & Li, W. (2020). Global View of Ionospheric Disturbance Impacts on Kinematic GPS Positioning Solutions During the 2015 St. Patrick's Day Storm. *Journal of Geophysical Research: Space Physics*, *125*(7), e2019JA027681. doi: https://doi.org/10.1029/2019JA027681

Yizengaw, E., Moldwin, M., Galvan, D., Iijima, B., Komjathy, A., & Mannucci, A. (2008). Global plasmaspheric TEC and its relative contribution to GPS TEC. *Journal of Atmospheric and Solar-Terrestrial Physics*, *70*(11-12), 1541–1548.

Zakharenkova, I., & Cherniak, I. (2021). Effects of storm-induced equatorial plasma bubbles on GPS-based kinematic positioning at equatorial and middle latitudes during the September 7–8, 2017, geomagnetic storm. *GPS Solutions*, *25*(4), 1–14. doi: https://doi.org/10.1007/s10291-021-01166-3

Zha, J., Zhang, B., Liu, T., & Hou, P. (2021). Ionosphere-weighted undifferenced and uncombined PPP-RTK: theoretical models and experimental results. *GPS Solutions*, *25*(4), 1–12.

Zhang, H., Gao, Z., Ge, M., Niu, X., Huang, L., Tu, R., & Li, X. (2013). On the Convergence of Ionospheric Constrained Precise Point Positioning (IC-PPP) Based on Undifferential Uncombined Raw GNSS Observations. *Sensors*, *13*(11), 15708–15725. doi: https://doi.org/10.3390/s131115708

Zhang, S.-R., Vierinen, J., Aa, E., Goncharenko, L. P., Erickson, P. J., Rideout, W., ... Spicher, A. (2022). 2022 Tonga Volcanic Eruption Induced Global Propagation of Ionospheric Disturbances via Lamb Waves. *Frontiers in Astronomy and Space Sciences*, *9*. doi: https://doi.org/10.3389/fspas.2022.871275

Zou, Y., & Wang, D. (2009). A study of GPS ionospheric scintillations observed at Guilin. *Journal of Atmospheric and Solar-Terrestrial Physics*, *71*(17-18), 1948–1958.

Zumberge, J. F., Heflin, M. B., Jefferson, D. C., Watkins, M. M., & Webb, F. H. (1997). Precise point positioning for the efficient and robust analysis of GPS data from large networks. *Journal of Geophysical Research: Solid Earth*, *102*(B3), 5005-5017. doi: https://doi.org/10.1029/96JB03860

# Supporting Information for "The ionospheric effects of the 2022 Hunga Tonga Volcano eruption and the associated impacts on GPS Precise Point Positioning across the Australian region"

B. A. Carter[1], R. Pradipta[2], T. Dao[1], J. L. Currie[1], S. Choy[1], P. Wilkinson[3], P. Maher[4,5], R. Marshall[4], K. Harima[6], M. LeHuy[7], T. Nguyen Chien[7], T. Nguyen Ha[7], T. J. Harris[8]

[1]School of Science, RMIT University, Melbourne, Australia

[2]Institute for Scientific Research, Boston College, Boston, USA

[3]Ionospheric Prediction Service (retired), Sydney, Australia

[4]Space Weather Services, Bureau of Meteorology, Sydney and Adelaide, Australia

[5]Now at: Riverbed Technology, Australia

[6]FrontierSI, Melbourne, Australia

[7]Institute of Geophysics, Vietnam Academy of Science and Technology (VAST), Hanoi, Vietnam

[8]School of Physical Sciences, The University of Adelaide, Adelaide, Australia

## Contents of this file



## Description of interactive maps S1, S2 and S3

Here we provide some additional interactive maps to supplement the figures presented in the main manuscript. The format is html, which is supported by internet browser

---

programs. While Figures 7, 9 and 10 in the main manuscript provide snapshots of the map of Australia, with the change in convergence time $\Delta T_C$, ROTI and $\langle VTEC \rangle$ data, S1, S2 and S3 here provide the reader with interactive maps to facilitate their own data exploration. Each map animates through time and is controllable with the slider at the bottom; S1 spans 0-18 UT, S2 spans 0-23:50 UT and S3 spans 07-16:45 UT on January 15, 2022. Further, the reader can zoom in and out of the maps plotted and click-and-drag to move around the map, and explore the plotted data points by hovering the mouse pointer over them. For reference, the location of Tonga is shown as the red cross, and the locations of the ionosonde stations are shown in S2 and S3 as black triangles.